

# Comparative Study of Transition Models for High Angle of Attack Behavior

Jolan Wauters\*, Joris Degroote<sup>†</sup> and Jan Vierendeels<sup>‡</sup>

*Ghent University, Ghent, Belgium*

*EEDT, Flanders Make*

This paper considers transition modeling for the flow over small unmanned aerial vehicles with a span of around 1 m. Such flows are characterized by very low values of turbulent intensity and the main cause for transition corresponds to flow separation. Four different turbulence models for low Reynolds number flow are compared with the experimental data for a NACA 0018 airfoil over a range of 2D as well as 3D conditions. The turbulence models under consideration are Menter's  $k - \omega$  SST model with Wilcox's low- $Re$  modification, Menter & Langtry's ( $k - \omega$  SST)  $\gamma - Re_\theta$  model along with its simplified version in the form of the ( $k - \omega$  SST)  $\gamma$  model, and Walters & Coklj'a's  $k - k_l - \omega$  model. The NACA 0018 profile is rotated in a flow with a chord-based Reynolds number of  $3 \times 10^5$  at three different rotational speeds between an angle of attack (AoA) of  $0^\circ$  and  $25^\circ$ . Using a curve fitting methodology, an estimate of the results at an infinitesimally slow rotation can be made. Both clockwise and counterclockwise rotations are considered to allow an assessment of the model for predicting steady hysteresis. Furthermore, 3D computations for an infinite wing are performed to examine the appearance of coherent structures at high AoA, namely, stall cells or low frequency fluctuations.

## Nomenclature

$c$	Chord length, [m]
$C_c$	Convective coefficient von Neumann stability analysis
$C_d$	Diffusive coefficient von Neumann stability analysis
$C_D$	Drag coefficient; $D/0.5\rho U_{ref}^2 c$ , [-]
$C_{decay}$	Decay constant
$C_L$	Lift coefficient; $L/0.5\rho U_{ref}^2 c$ , [-]
$C_M$	Moment coefficient; $M/0.5\rho U_{ref}^2 c^2$ , [-]
$C_P$	Pressure coefficient; $P/0.5\rho U_{ref}^2$ , [-]
$D$	Drag, [N]
$f_v$	Frequency of vortex shedding, [ $s^{-1}$ ]

$F$	Spatial function
$F_c$	Discrete spatial convective operator
$F_d$	Discrete spatial diffusive operator
$G$	Gain/Amplification factor, [-]
$j$	Imaginary unit
$k$	Turbulent kinetic energy, [ $m^2/s^2$ ]
$k_l$	Laminar kinetic energy, [ $m^2/s^2$ ]
$L$	Lift, [ $N$ ]
$M$	Moment, [ $Nm$ ]
$P$	Static pressure, [ $Pa$ ]
$r$	Wall normal expansion ratio, [-]
$R_T$	Turbulent viscosity ration; $\mu_t/\mu$ , [-]
$Re_c$	Chord-based Reynolds Number; $\rho U_{ref} c / \mu$ , [-]
$Re_T$	Turbulent Reynolds number; $\rho k / \mu \omega$ , [-]
$Re_\theta$	Momentum-thickness Reynolds number; $\rho U_{ref} \theta / \mu$ , [-]
$s$	Span, [ $m$ ]
$S_0, S_1$	Source term
$St$	Strouhal number; $f \lambda / U_{ref}$ , [-]
$Tu$	Turbulent intensity, [-]
$u$	Local velocity, [ $m$ ]
$U_{ref}$	Free-stream velocity, [ $m/s$ ]
$x$	Chordwise position, [ $m$ ]
$y^+$	Distance in wall coordinates; $\rho y u_\tau / \mu$ , [-]
$\#n_c$	Number of nodes on chord, [-]

#### *Greek*

$\gamma$	Intermittency, [-]
$\Gamma$	Diffusity constant
$\lambda_L$	Characteristic length, [ $m$ ]
$\mu$	Dynamic viscosity of air, [ $kg/ms$ ]
$\mu_t$	Turbulent/eddy viscosity, [ $kg/ms$ ]
$\omega$	Specific turbulence dissipation rate, [ $1/s$ ]
$\omega_{deg}$	Rotational speed, [ $^o/s$ ]

$\omega_F$	Fourier decomposition wave number
$\phi$	Transported scalar
$\phi_{\omega_F}$	Fourier decomposition wave amplitude
$\rho$	Density of air, [ $kg/m^3$ ]
$\theta_F$	Fourier decomposition wave angle

#### *Subscript*

<i>Inlet</i>	Value at inlet computation domain
--------------	-----------------------------------

#### *Acronyms*

<i>AoA</i>	Angle of Attack, [ $^\circ$ ]
<i>AR</i>	Aspect Ratio; s/c, [-]
<i>RANS</i>	Reynolds-Averaged Navier-Stokes
<i>UAV</i>	Unmanned Aerial Vehicle

## I. Introduction

THE widespread use of unmanned aerial vehicles (UAV) has become clear over recent years, thanks to its increasing ability to be deployed for a series of comprehensive tasks: from the more well known military up to and including its humanitarian counterpart. This has led to an enormous research boost in that field. In order to improve endurance, range, efficiency and the payload capacities of the drones, a deep understanding and correct modeling of the aerodynamic behavior is fundamental, which in turn may lead to the development of new aerial structures with a decreased drag force, increased lift force, delayed stall angle, reduced noise and vibrations, further extending its capabilities. Within the extensive range of UAVs that exists nowadays, this paper focuses on those that operate at a chord-based Reynolds numbers ( $Re_c$ ) below  $5 \times 10^5$ , the condition which is referred to as *low Reynolds number flow* [1].

Airfoils, with an adverse pressure gradient on the suction side, operating at low Reynolds numbers in external flow conditions, typically with low values of turbulence intensity, are characterized by the appearance of a transitional separation bubble (Figure 1). This bubble is often detrimental to the performance of the airfoil and is preferably avoided (for example by means of turbulators and bubble ramps). It is nevertheless of importance to correctly resolve this phenomenon to assure a correct estimation of the flight behavior of the UAV.

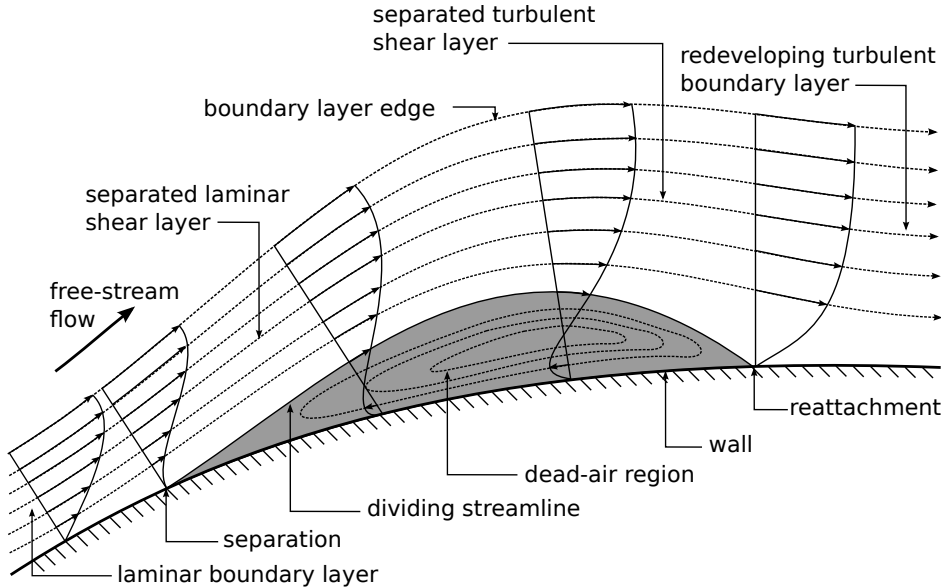


**Fig. 1 Separation bubble**

The relatively low computational cost that is attributed to Reynolds-Averaged Navier-Stokes (RANS) simulations allows its use in increasingly complex 3D geometries. The assumption of a fully turbulent flow that goes hand in hand with classic turbulence models, makes their use in low Reynolds applications somewhat ambiguous. The last couple of decades have however seen the birth of a number of turbulence models that attempt to model the transition phenomena that are attributed to low Reynolds number flow. Over recent years, the modeling of transitional flow with RANS simulations became increasingly more important and this has led to its implementation in commercial software. The transition models that were created to simulate this phenomenon were often designed to accurately represent the transition from laminar to turbulent flow for specific cases, such as bypass transition over a compressor blade [2], natural transition over a flat plate, wake-induced transition over a cascade [3] or hypersonic/supersonic transition through Mack instabilities [4]. Here it is attempted to evaluate the reliability of some of these models for the assessment of the high angle of attack (AoA) behavior of airfoils operating in low Reynolds, external flow conditions.

Based on the manner by which transition is predicted, transition models can be categorized as low Reynolds models, which make use of damping functions, correlation based models, which typically relate the production of intermittency to correlations depending on flow parameters, and physics-based models, which attempt to model the flow based on a more theoretical framework. Of the three categories, representatives are selected that are compared with each other to assess their abilities: firstly Menter's  $k - \omega$  Shear Stress Transport (SST) model [5] with Wilcox's low Reynolds modification [6], which belongs to the low Reynolds models, secondly Menter and Langtry's  $\gamma - Re_\theta$  model [7], thirdly Menter and Langtry's  $\gamma$  model [8], the former two belonging to the correlation models, and fourthly and finally Walter & Cockljat's  $k - k_l - \omega$  model [9], which is a physics-based model. A comparative study of these models presented in

2D for the prediction of high AoA and steady hysteresis behavior is given in §2. Comparison with experimental data brings forth discrepancies, which are further investigated in 3D in §3.

While numerous comparative studies have been devoted to transition model for a series of test cases, chord-based Reynolds number and turbulence intensity ranges [10–12], no light has as of yet been shed on the abilities of these models for the prediction of steady hysteresis. The importance in a correct modeling of static/steady hysteresis for UAV applications is for example found in the prediction of stall/spin recovery, which up until today can lead to a complete loss of aerial systems. It is also essential in the assessment of post-stall maneuverability, a particular requirement of small UAVs that typically do not have a landing gear but perform a belly landing an AoA with stall. Therefore, this paper will attribute to the list of comparative studies by its assessment of the aforementioned. Furthermore, the evaluation of models up until now has always occurred in a set of discrete points, which makes the prediction of burst\* only accurate up to the interval size. Here, a methodology is presented for a continuous assessment of the predictive capabilities of these models as a function of the angle of attack. Finally, experimental results have shown the strong 3D nature of the flow, especially at high angles of attack, to which, up until now, only little importance has been attached in the development of RANS models. Therefore, the difference in patterns for both 2D and 3D flows will be laid bare.

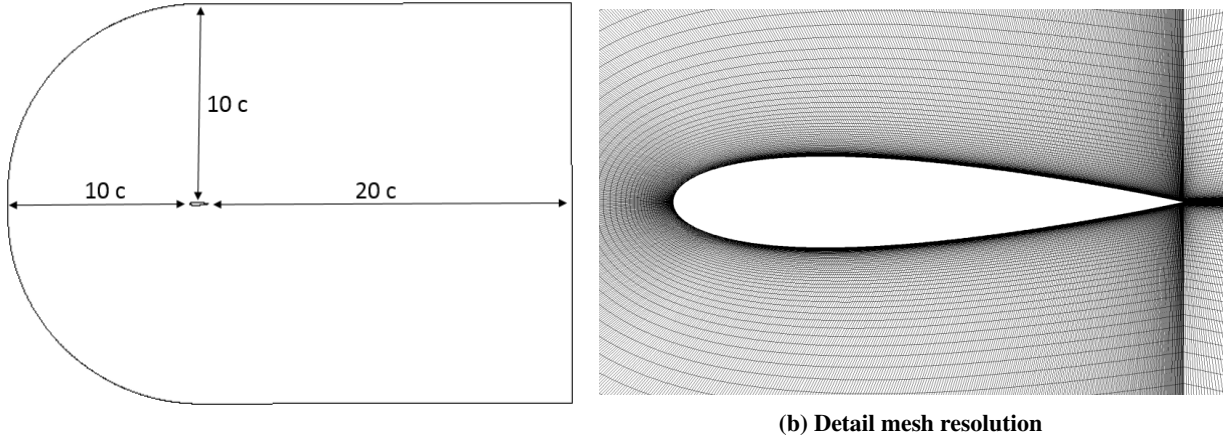


**Fig. 2 Computational domain**

## II. 2D Study

The comparative study of the transition models is presented by studying their capabilities to predict the increased lift caused by the separation bubble at lower AoAs, the abrupt burst of the separation bubble and the accompanied stall

---

\*Burst is defined as the point at which the separated shear layer is unable to reattach, leading to a fully separated flow over the airfoil, accompanied by an abrupt decrease of  $C_L$  and  $C_M$  and increase of  $C_D$  [13]. This phenomenon is closely related to trailing edge stall, also referred to as mild stall, encountered on thick airfoils and characterized by the separation of the trailing edge which grows towards the leading edge until it reaches the bubble which results in its bursting [14, 15].

at higher AoAs and the ability to predict steady hysteresis<sup>†</sup>. To do this the NACA 0018 profile is rotated around its mid-chord position at three different rotational speeds,  $\omega_{deg}$ :  $1^\circ/s$ ,  $0.5^\circ/s$  and  $0.1^\circ/s$  from  $0^\circ$  to  $25^\circ$ . This allows an exponential fitting (see section II.D) of the  $C_L$ -,  $C_D$ - and  $C_M$ -characteristics and predicts the behavior of a steady simulation for any AoA between  $0^\circ$  and  $25^\circ$ . By doing this the effect of unsteady hysteresis<sup>‡</sup> is eliminated. The same procedure is followed by rotating counterclockwise from  $25^\circ$  to  $0^\circ$ . Placing the characteristics on top of each other will directly provide a quantitative measurement of the ability of the transition models abilities to predict hysteresis.

Since the NACA 0018 is a symmetric profile, the aerodynamic center is to be found at  $\frac{1}{4}$  of the chord. However, the appearance of a separation bubble both on the suction (upper) and pressure (lower) side changes the shape of the airfoil by introducing an artificial chamber, as it were. A study of the  $C_M$ -characteristic will then allow, without the need to consider the  $C_P$ -distribution, the assessment of how the separation bubbles move on the surface.

### A. Boundary Conditions

The simulations are performed in such a way that they allow the comparison with the experimental measurements of Timmer [19] for  $Re_c = 3 \times 10^5$ . The measurements were executed in the Delft University Wind Tunnel using a  $0.25m$  chord model at velocities ranging between  $10m/s$  and  $70m/s$  with respectively corresponding  $Tu$  ( $= \sqrt{2k/3}/U$ ) values of  $0.02\%$  and  $0.07\%$ . This results in  $Tu = 0.04\%$  for  $Re_c = 3 \times 10^5$ .

From the experimental studies and the trigger functions in the transition models discussed before, it can be noted that  $Tu$  is a dominant parameter. RANS modeling has been characterized by a decay of  $Tu$  especially for external flows, predominantly found in aeronautical applications. This decay of  $Tu$  is caused by the fact that only the destruction terms in the  $k$  and  $\omega$  transport equations are active between inlet and leading edge [20]. In order to predict the value of  $Tu$  at the inlet of the computational domain that one may obtain a  $Tu = 0.04\%$  at the leading edge, the decay can be calculated from the decay of  $k$  for the  $\gamma - Re_\theta$  model<sup>§</sup>:

$$k = k_{inlet}(1 + \omega_{inlet}C_{decay}t)^{\frac{-C_{decay}^*}{C_{decay}}} \quad \text{with} \quad C_{decay} = 0.09 \quad \text{and} \quad C_{decay}^* = 0.0828 \quad (1)$$

A time scale can be determined as follows:  $t = x_{inlet}/U_{ref}$ , where  $x_{inlet}$  is the streamwise distance downstream of the inlet and  $U_{ref}$  is the mean convective velocity. The turbulent viscosity in case of the  $k - \omega$  SST model is defined as:  $\mu_t = \rho k / \omega$ . The decay of turbulent kinetic energy equation can be rewritten in terms of inlet turbulent intensity ( $Tu_{inlet}$ ) and inlet turbulent viscosity ratio,  $(\mu_t/\mu)_{inlet}$ , as follows:

---

<sup>†</sup>With steady hysteresis we refer to the phenomenon of history dependency of aerodynamic characteristics on the sense change of the AoA [16]. Williams and colleagues use the term *static* [17]

<sup>‡</sup>With unsteady hysteresis we refer to the phenomenon of history dependency of aerodynamic characteristics on the speed of change of the AoA [18]. Williams and colleagues use the term *dynamic* [17]

<sup>§</sup>The decay behaves differently depending on the model, consequently the provided formula then only serves as an indicator and must be checked afterwards

$$Tu(x_{inlet}) = \left( Tu_{inlet}^2 \left[ 1 + \frac{3\rho U_{ref} x_{inlet} C_{decay} (Tu_{inlet}^2)}{2\mu(\mu_t/\mu)_{inlet}} \right]^{\frac{-C_{decay}^*}{C_{decay}}} \right)^{0.5} \quad (2)$$

Spalart & Rumsey [20] recognized the relevance of turbulent decay and the difficulty in defining a reasonable combination of  $Tu_{inlet}$  and  $\mu_t/\mu$  that would yield acceptable results. They proposed for aeronautical applications the following relation:  $\mu_t/\mu \approx 2 \times 10^{-7} \times Re_c$ , which yields for  $Re_c = 3 \times 10^5$  the following:  $\mu_t/\mu = 0.06$ . Using Equation 2 with  $(\mu_t/\mu)_{inlet} = 0.06$ ,  $Tu_{inlet} \approx 0.23\%$ <sup>¶</sup>. Larger values of  $(\mu_t/\mu)_{inlet}$  lead to a slower decay, but may influence the flow field.

## B. Numerical Parameter Study

The computational domain surrounding the airfoil is *c*-shaped: extending 10 chord lengths in front, above and below the airfoil and 20 chord lengths behind<sup>¶</sup> it as presented in Figure 2a. Following the strict requirements of the mesh for the transition models [7, 8, 21], a minimum wall normal expansion ratio of 1.1 should be imposed on the 100 layers surrounding the airfoil to obtain a  $y^+$  of maximum 1 near the stagnation point and on average 0.35. All calculations are performed using CFD-code ANSYS Fluent 16.2 with a second-order upwind for convective terms, second-order central for diffusive terms, gradient least squares cell based discretization, a transient second-order implicit formulation and the SIMPLE pressure-velocity coupling. During every time-step the scaled residuals decrease to  $10^{-5}$  using a scaling factor representative of the flow rate of the quantity of interest through the domain<sup>\*\*</sup>

Chordal grid discretization,  $\#n_c$ , time step size,  $\Delta t$ , wall normal expansion ratio,  $r$  and first cell size,  $y^+$ , were subjected to a comparative study displayed in Figure 3. In order for the grid discretization error not to influence the comparative study of the time step size, and vice versa, the finest grid, respectively the smallest time step, is chosen to study the influence of the other numerical parameters. The experimental measurement of Timmer [19] for  $C_D(AoA = 0)$  is displayed as a reference for the different cases.

<sup>¶</sup>Different combinations of  $(\mu_t/\mu)_{inlet}$  and  $Tu_{inlet}$  that produce the desired  $Tu$  at the leading edge are possible. These have a negligible influence on the quantities of interest:  $(\mu_t/\mu)_{inlet} = 6$  leads to a 1% change in  $C_D$

<sup>\*\*</sup>A numerical study towards the sensitivity of the flow domain was also performed and showed that by increasing each dimension five fold the  $C_D$  changes on average 0.1%. Therefore the results, being so close to each other, are not depicted here.

<sup>\*\*</sup>Converging to  $10^{-6}$  only changes the quantities of interest with  $< 0.1\%$ , but significantly increases the computational time, therefore it is judged that  $10^{-5}$  is an appropriate criterion.

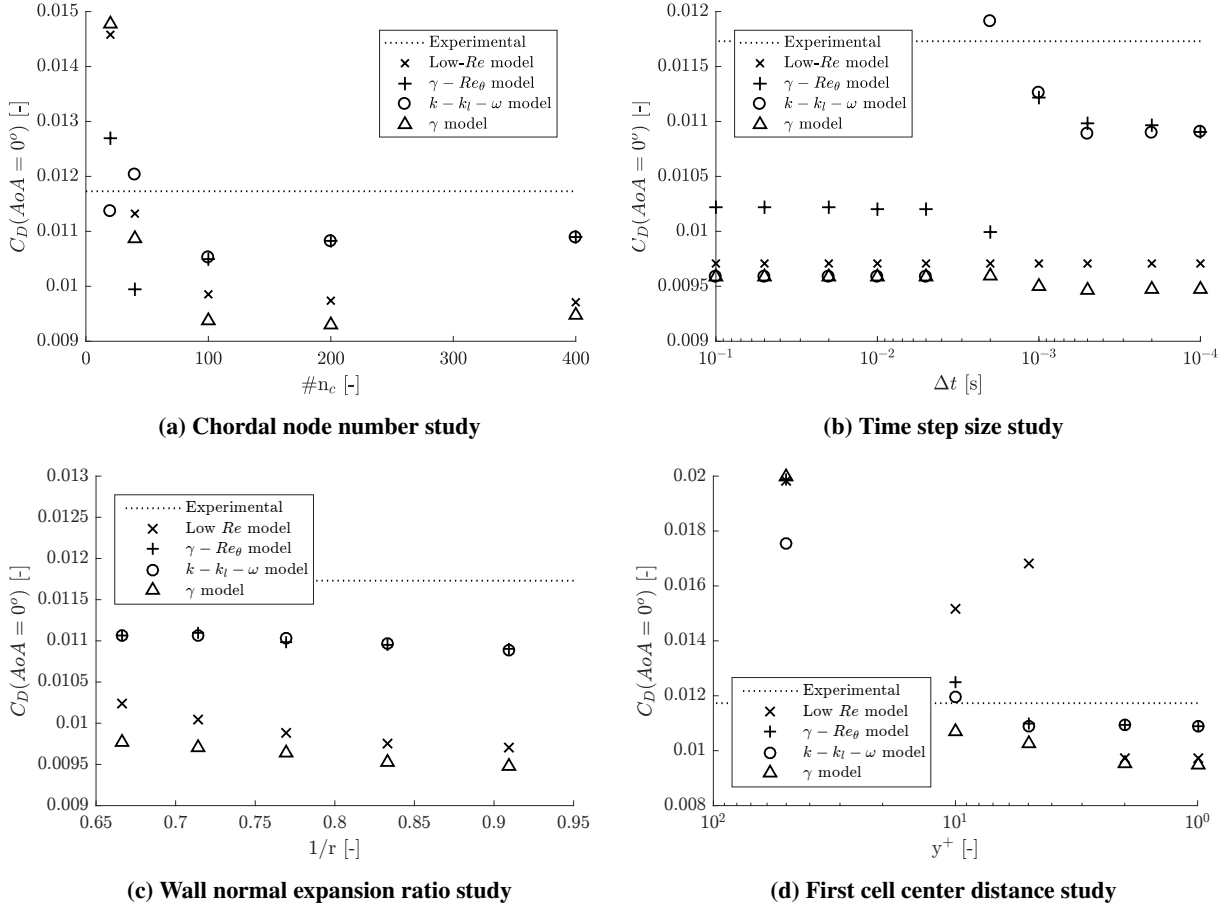


**Fig. 3 Numerical parameter study in 2D**

First of all it can be seen from figure 3b that at  $AoA = 0$   $C_D$  is independent of  $\Delta t$  for the low- $Re$  model since it predicts a steady value. The other transition models clearly predict some kind of transition when crossing  $\log_{10}(1/\Delta t) \approx 2.5 - 3$ . This transition is attributed to the appearance of vortex shedding in the lower range of time steps (towards the right of the figure). A *von Neumann stability analysis* (see the Appendix) shows the behavior of the discretization schemes used as filters with increasing  $\Delta t$ . Depending on the transition model used, some transition related vortices are resolved. This might seem counterintuitive from a RANS perspective, which builds on the modeling of turbulence. In that sense, these transition models move towards LES and are somewhat similar to SAS from the perspective of resolving part of the transition (turbulence) related structures. The consequence is that flows, which would be steady by conventional turbulence models, now become unsteady using transition models. The von Neumann analysis shows how the implicit second order scheme filters the highest frequencies of these structures. This implies that by increasing the time step, a steady solution can be obtained. However, this steady solution deviates from the time-averaged unsteady solution.

While there is a difference between steady and unsteady results of  $C_D(AoA = 0^\circ)$  for the different transition models,

the maximal difference is  $\Delta C_D \approx 20$  drag counts. The  $k - k_l - \omega$  and  $\gamma - Re_\theta$  models predict the experimental value of  $C_D$  most correctly. The  $\gamma$  model, which most strongly under-predicted  $C_D$ , still performs well since  $\Delta C_D \approx 20$  drag counts.

It was discussed above that even when the vortex shedding is not resolved, the  $C_D$  is still well predicted. So even when the bubble decreases in size when the AoA increases and the time step remains the same, it is expected that the predicted  $C_D$  will still give a reasonable result. However, when the  $\#n_c$  decreases below 100, the separation point on the pressure and suction side moves upstream resulting in a larger turbulent boundary layer and subsequently a much larger  $C_D$ . It is thus expected that the burst behavior will be wrongfully predicted for a mesh that is too coarse. The transition models clearly show an exponential growth in  $C_D$  with decreasing  $\#n_c$ . With increasing  $y^+$  the point of separation moves upstream. For larger expansion factors, which corresponds with a decrease of cells in the boundary layer<sup>††</sup>, there is an upstream shift in the transition location, because the sensitivity of the solution to wall-normal mesh resolution can increase for flows with pressure gradients.

For the remainder of the study the finest grid dimensions and time step that were evaluated during the numerical parameter study will be used: 400 nodes along the chord, a wall normal expansion ratio equal to 1.1,  $y^+$  equal to 1 and a time step size equal to  $10^{-4}$ .

### C. Central Value

As mentioned in previous section, the  $\gamma - Re_\theta$ ,  $\gamma$  and  $k - k_l - \omega$  models are characterized by unsteady behavior due to a periodic vortex shedding from the separation bubble, in literature described as breathing or flapping [22], when the grid size and time step size decrease below certain threshold values. Since the mesh is rotated as a function of time it is not possible to obtain a time averaged  $C_L$ -,  $C_D$ - and  $C_M$ -value for every AoA. An alternative approach would be to rotate the mesh various times starting from a different initial state, thus obtaining multiple  $C_L$ -,  $C_D$ - and  $C_M$  for every AoA and averaging these out. However, the high computational cost that at this point is already consumed by the fine grid, small time step size and slow rotational speed does not allow this approach. Instead a single value is obtained by estimating the boundaries of the  $C_L$ -,  $C_D$ - and  $C_M$ -fluctuations and taking the central value between the boundaries. This is done by taking the maximum and minimum value in fixed intervals. These points are connected to form a piecewise linear curve, respectively corresponding to the upper and lower boundary. The high frequency of vortex shedding and the low rotational velocity allows the use of small intervals, which produces a much smoother curve. The approach is illustrated in Figure 4 for the clockwise and counterclockwise rotation using the  $\gamma - Re_\theta$  model at a speed of  $1^\circ/s$ .

---

<sup>††</sup>For each of the meshes examined here, the maximum  $y^+$  value is equal to 1, consequently, a change in wall normal expansion ratio changes the number of cells in the boundary layer: at  $x/c = 0.5$ , just before the boundary layer separates we have at  $1/r = 0.909$  24 cells in the boundary layer, at  $1/r = 0.833$  17 cells, at  $1/r = 0.769$  14 cells, at  $1/r = 0.714$  11 cells and at  $1/r = 0.667$  9 cells.

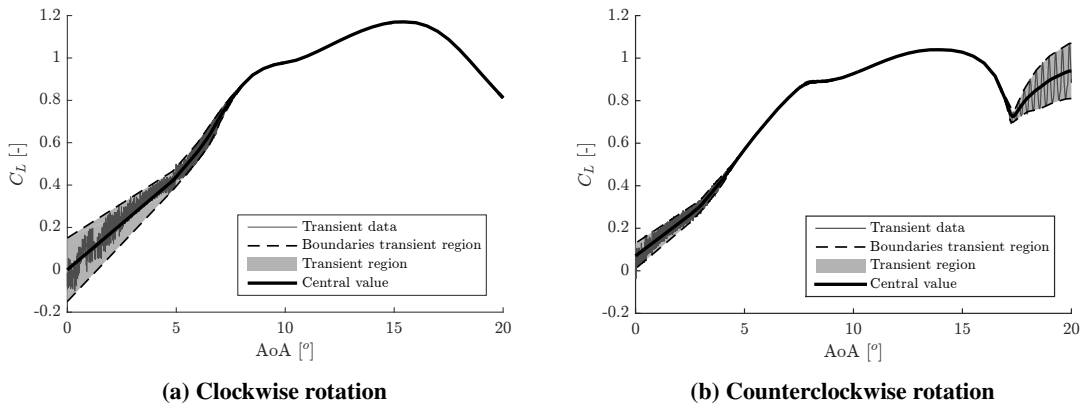


**Fig. 4** Central value of  $C_L(AoA)$ -characteristic of the  $\gamma - Re_\theta$  model rotating at  $\omega_{deg} = 1^\circ/s$

## D. Exponential Fitting

The rotational speed leads to an unsteady hysteresis behavior as discussed before. In order to assess the steady hysteresis, it needs to be isolated. This is done through the estimation of the  $C_L$ -,  $C_D$ - and  $C_M$ -characteristics at an infinitesimally slow rotational speed: by rotating the profile at three different speeds ( $1^\circ/s$ ,  $0.5^\circ/s$  and  $0.1^\circ/s$ ) the central value at every AoA for the three curves can be fitted to an exponential curve:  $a \exp(bx) + c$ , with  $x = \omega_{deg}^{-1}$ . It is expected that  $b$  will be negative, so that the exponential component goes to zero and  $c$  becomes the coefficient of interest for  $\omega_{deg} \rightarrow 0$ . The approach is illustrated in Figure 5.

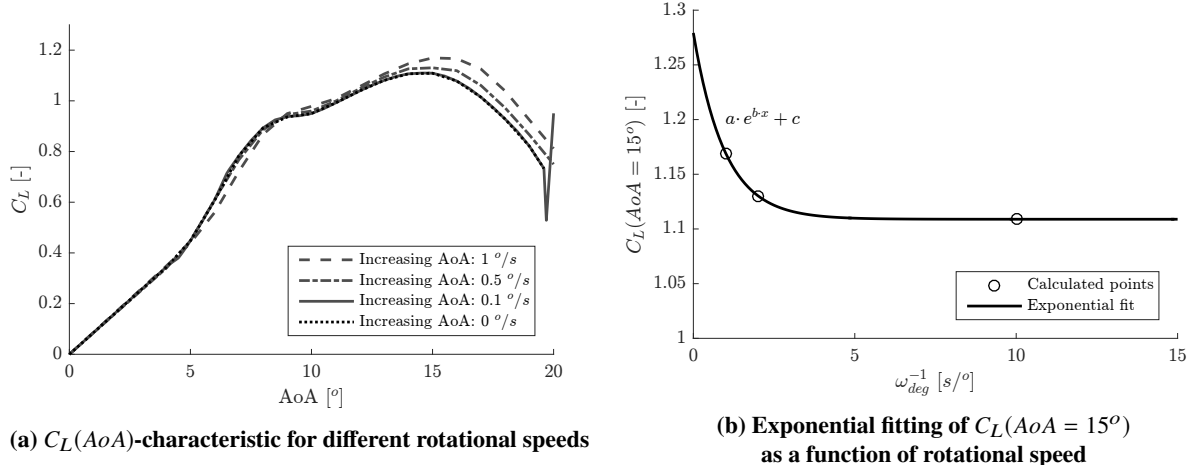
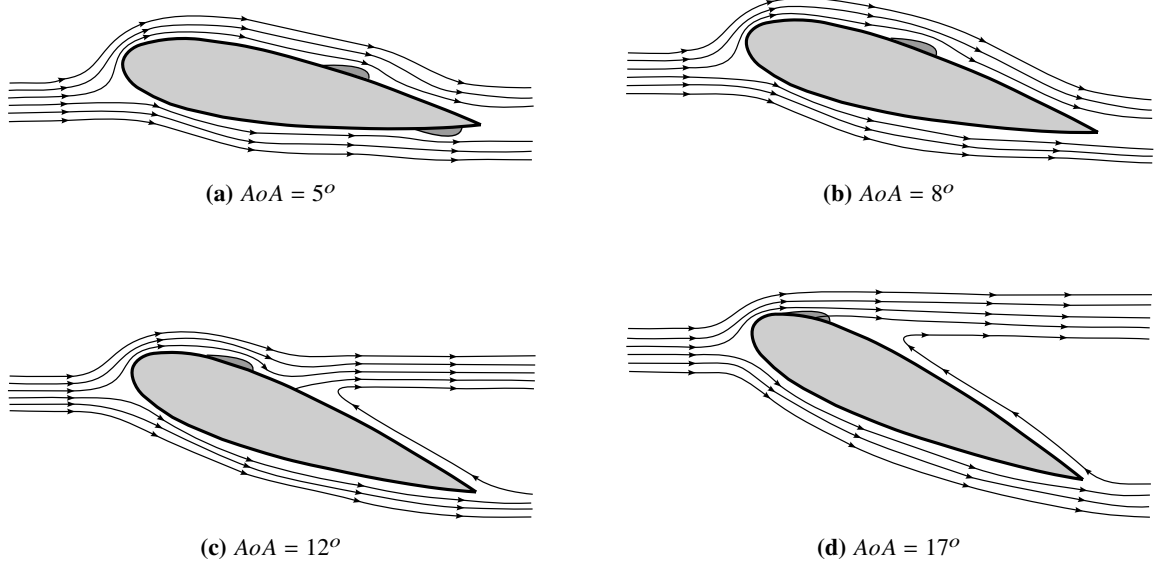


**Fig. 5 Fitting Strategy with the  $\gamma - Re_\theta$  model**

## E. Results

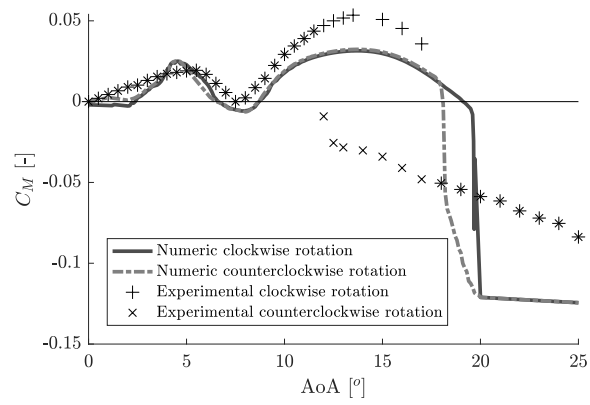
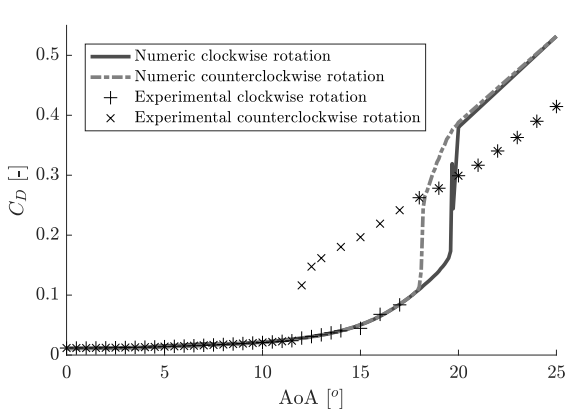
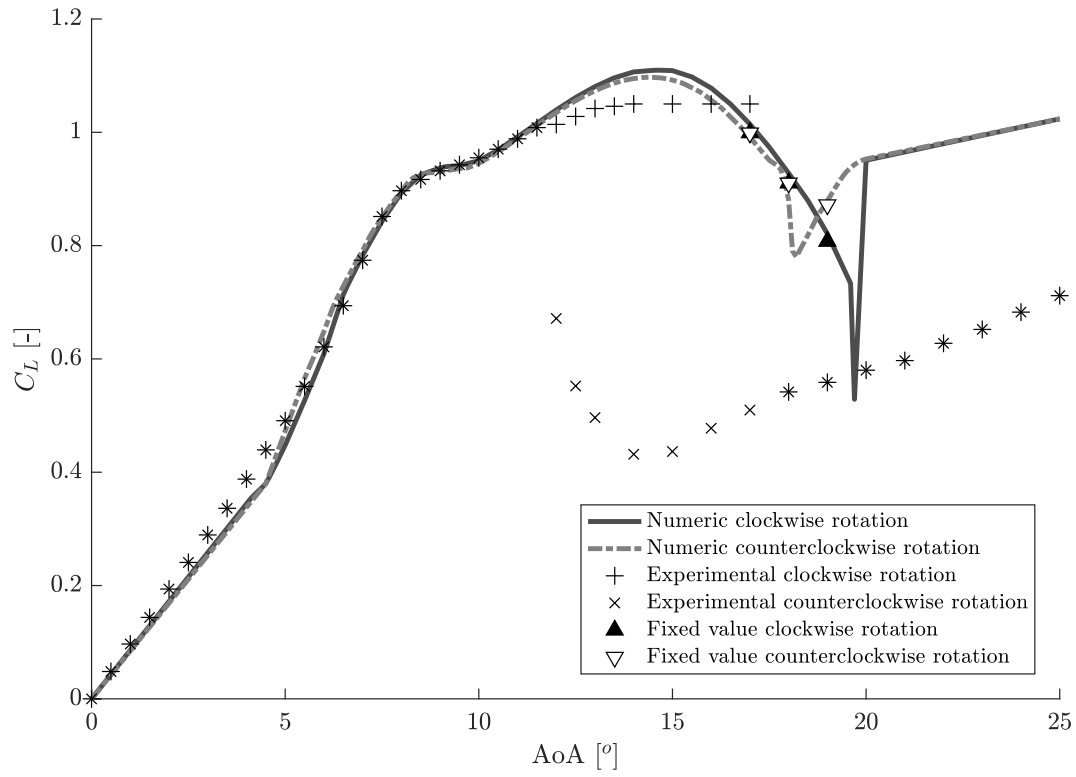
First, a more in depth comparison of the results of the  $\gamma - Re_\theta$  model with experimental data of the  $C_L$ -,  $C_D$ - and  $C_M$ -characteristics (Figure 7) is presented, after which the characteristics of the different transition models are placed next to each other.

Figure 7a shows the  $C_L$ -characteristic of the  $\gamma - Re_\theta$  model, both for an infinitesimally slow rotation in clockwise as in counterclockwise direction along with the experimental measurements of Timmer [19]. In clockwise rotation it can be noted that the model predicts the characteristic trustworthy up to  $12^\circ$ , after which a slight overestimation of the lift is to be found up to the experimental burst angle  $\approx 17^\circ$ .



**Fig. 6 Schematic representation of the separation bubble movement for changing AoA [23].**

This first part,  $AoA = 0^\circ - 17^\circ$ , can be experimentally divided in three regions. The first, extending from  $AoA = 0^\circ - 5^\circ$ , is characterized by a linear increase of  $C_L$ , similar to a fully turbulent flow. On both the pressure and suction side a separation bubble is found that produces an alternating vortex shedding in the shape of a *von Karman vortex sheet* (Figure 6a). As the angle of attack increases the bubble on the suction side moves upstream and the bubble on the pressure side moves downstream. The appearance of the separation bubbles introduces a pressure plateau and can intuitively be understood as a change in shape of the airfoil itself. While this affects  $C_M$  most strongly, the influence on  $C_L$  is minimal in this first region since the pressure plateaus compensate each other. The ‘change’ of the profile shape introduces a positive  $C_M$  that increases with AoA. At an  $AoA = 5^\circ$  the bubble on the pressure sides reaches the trailing edge and disappears into the wake. The pressure plateau on the suction side now adds to the  $C_L$  and leads to an, as we will call it, ‘over-linear’ increase of  $C_L$  up to  $AoA = 8^\circ$  (Figure 6b).  $C_M$  also decreases since the bubble on the suction side is still found behind the  $1/4$ -chord point and moves upstream with increasing AoA, reaching the quarter chord position at  $AoA = 8^\circ$  leading to a  $C_M = 0$ . As the AoA increases past  $AoA = 8^\circ$ , the trailing edge starts to separate, undermining the growth of  $C_L$ , which is also aided by the decreasing bubble size with increasing AoA (Figure 6c).  $C_M$  again starts to increase in this region, since the bubble passed the quarter chord point and the trailing edge separates leading to a nearly constant pressure from the trailing edge upstream to the point of separation.  $C_D$  is also characterized by a stronger increase.



**Fig. 7 Comparison of the characteristics predicted by the  $\gamma - Re_\theta$  model with experimental data [19]**

Experimentally, the bubble bursts before separation reaches the reattachment point (Figure 6d). However, this is not the case for the  $\gamma - Re_\theta$  model where numerically the lift coefficient drops more gradually, caused by the upstream movement of trailing edge separation, as found in fully turbulent flows for thick profiles. The numerical burst of the bubble is delayed up to  $\approx 19.5^\circ$  after which there is a slight drop of the  $C_L$  of  $\Delta C_L \approx 0.2$  followed by a fast recovery of lift,  $C_L(AoA = 20^\circ) \approx 0.95$ .

While rotating in counterclockwise direction, experimentally, it can be noted that the flow remains detached up to  $AoA = 12^\circ$ . After which the flow reattaches and forms a closed hysteresis loop. Further decreasing the AoA results in the same behavior as a clockwise rotation. Numerically the flow reattaches much faster, at  $AoA = 18^\circ$ , forming a numerical hysteresis loop of no more than  $\approx 2^\circ$ . In order to assess the correctness of the approach, the clockwise and counterclockwise rotation was stopped and held stationary in the experimental clockwise burst angle:  $AoA = 17^\circ$ , the numerical counterclockwise reattachment angle:  $AoA = 18^\circ$  and in the middle of the numerically predicted hysteresis loop:  $AoA = 19^\circ$ . At  $AoA = 17^\circ$  and  $18^\circ$  both the clockwise and counterclockwise rotation held stationary predict the same value. For example: at  $AoA = 17^\circ$  we obtain for a value of 1.0144 for  $c$  in the fitting of  $C_L$ , while the CFD value of  $C_L$  in the absence of rotation is 0.9991, which corresponds with an error of 1.5%. Furthermore, the difference between the CFD value and the experimental value is 5.1%. From this it is deemed that the method performs satisfactory. The slight difference in the two characteristics can thus be attributed to a lingering unsteady hysteresis effect. However  $AoA = 19^\circ$  shows distinctly different values.

The  $C_L$ -behavior in time (Figure 9a) and the time-averaged pressure distribution (Figure 9b) show the distinctively different behavior of the flow at the same AoA. In clockwise direction a steady value in time can be seen, while in reverse direction a periodic behavior is visible, which can be attributed to a vortex shedding of the leading edge. In case of the latter the airfoil acts as a blunt body with a Strouhal number,  $St = f\lambda_L/U_{ref}$  with  $f$  the vortex shedding frequency and  $\lambda_L$  the characteristic length (roughly equal to the projection of the airfoil perpendicular to the free-stream:  $c \times \sin(AoA)$ ), equal to 0.19. This corresponds to  $St$  of a cylinder for the same  $Re_c$ .

Furthermore, a noteworthy observation is the *lemniscate*-like shape of the hysteresis loop (Figure 7a,  $AoA = 18^\circ - 20^\circ$ ). This feature can be attributed to the fact that  $C_L$  is characterized by a very fast recovery following the burst. This abrupt remount is unphysical and strongly undermines the credibility of the transition model for high AoA. In this regard it can be stated that the  $\gamma - Re_\theta$  model is capable of predicting burst and hysteresis, but the former too late and the latter in an unphysical manner.

In regards to the behavior of  $C_D$  (Figure 7b) the same conclusions can be drawn as from the  $C_L$ -behavior. In the authors' opinion the prediction of  $C_M$  (Figure 7c) is undervalued in the assessment of transition models: in the case of UAVs the value of  $C_M$  will influence the position of the control surfaces. Tailless configurations are characterized by larger surfaces and/or bigger deflections. This will impact the values of  $C_L$  and  $C_D$  to a much bigger extent and possibly lead to a different burst angle for large AoAs. A correct prediction of the behavior of  $C_M$  is thus fundamental in the

correct simulation of UAVs. The  $\gamma - Re_\theta$  model correctly predicts the trend of  $C_M$ , characterized by an increase up until  $5^\circ$ , caused by the counterclockwise movement of the separation bubble on the pressure side and clockwise movement on the suction side, followed by a decrease up until  $8^\circ$ , caused by the disappearance of the separation bubble into the wake on the pressure side. The maximum value of  $C_M$  (Figure 7c,  $AoA = 5^\circ$ ) is however too large, demonstrating that the pressure plateau caused by the bubble is overestimated, and predicted too early, indicating that the separation bubble is found far downstream. This is also visible in the  $C_L$ -distribution (Figure 7a), where the nick is found numerically at  $5^\circ$  and experimentally at  $6^\circ$ . Up to the experimental hysteresis loop ( $AoA = 12^\circ$ ), the experimental and numerical value correspond quite well, after which a discrepancy is visible, also notable in the  $C_L$ -characteristic:  $C_M$  is numerically under-predicted and  $C_L$  over-predicted. It is believed that at this point experimentally the separation bubble reaches the leading edge and undermines the suction peak, stagnating the growth in  $C_L$  and increasing  $C_M$ . Numerically this does not happen, which causes  $C_M$  to stagnate and  $C_L$  to further increase, yet more slowly from  $AoA = 8^\circ$  onwards, at which point separation from the trailing edge starts to occur.

When comparing the  $C_L$ -characteristics predicted by the different transition models in clockwise (Figure 10a) and counterclockwise direction (Figure 10b) a first remark will be made in reference to the  $k - k_l - \omega$  model. For the lower  $AoA$ -range ( $0 - 8^\circ$ ) it can be noted that the model correctly predicts the separation bubble and its movement on the surface by considering the linear and over-linear growth of  $C_L$ . However, once separation from the trailing edge is expected to appear ( $AoA = 8^\circ$ ), the model's prediction deviates from the experimental value by upholding an attached flow near the trailing edge up until  $AoA = 13^\circ$ , at which point a more sudden separation of the boundary layer occurs. The term burst is deliberately not used here since this phenomenon does not influence the separation bubble. With a further increase of the AoA, the point of separation moves upstream, but nevertheless is found on a more downstream position compared with the other turbulence models. This explains why no burst is to be found below  $AoA = 20^\circ$ . Furthermore, the suction peak is far bigger than for the other transition models, explaining the overestimation of  $C_L$  (Figure 8a). Based on these results, the  $k - k_l - \omega$  model will be left out of further comparisons.

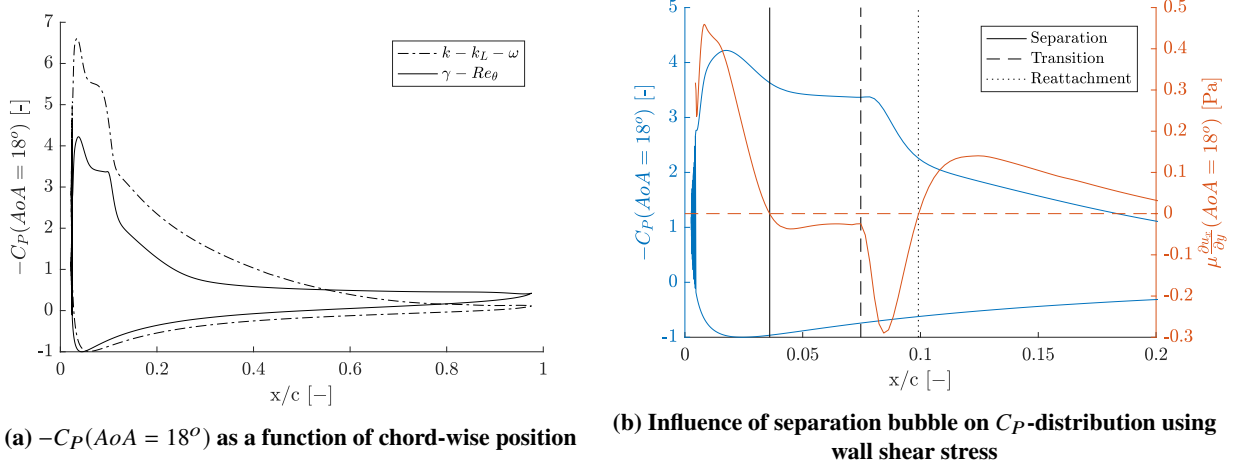


**Fig. 8** Assessment of the high AoA prediction of the  $k - k_L - \omega$

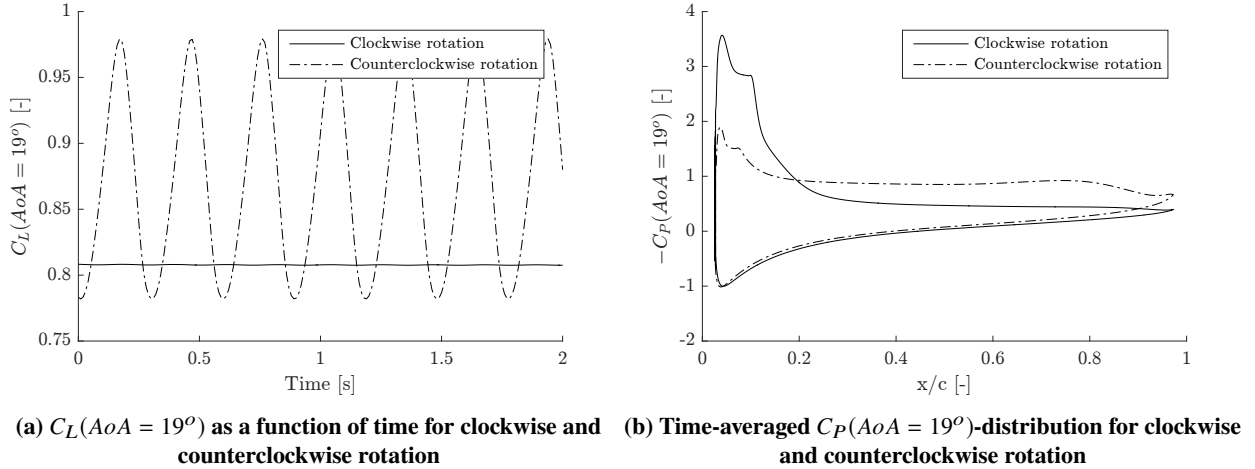


**Fig. 9** Assessment of hysteresis predicted by the  $\gamma - Re_\theta$  model at  $AoA = 19^\circ$

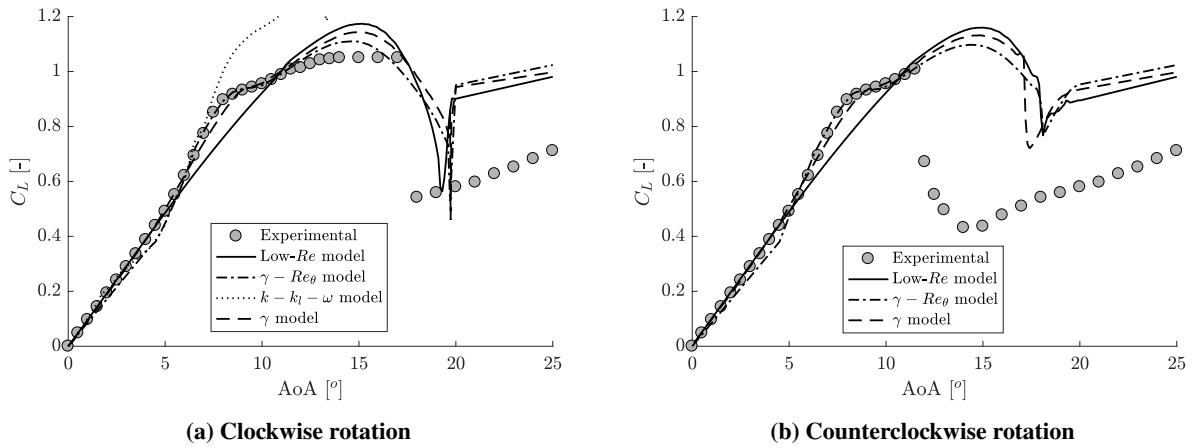


**Fig. 10 Comparison of the  $C_L(\text{AoA})$ -characteristics predicted by the models with experimental data [19]**

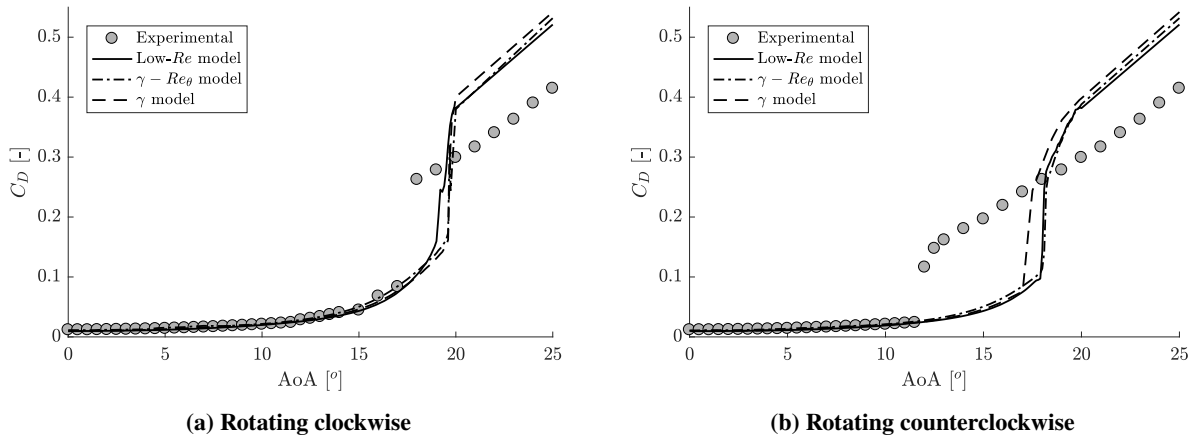


**Fig. 11 Comparison of the  $C_D(\text{AoA})$ -characteristics predicted by the models with experimental data [19]**

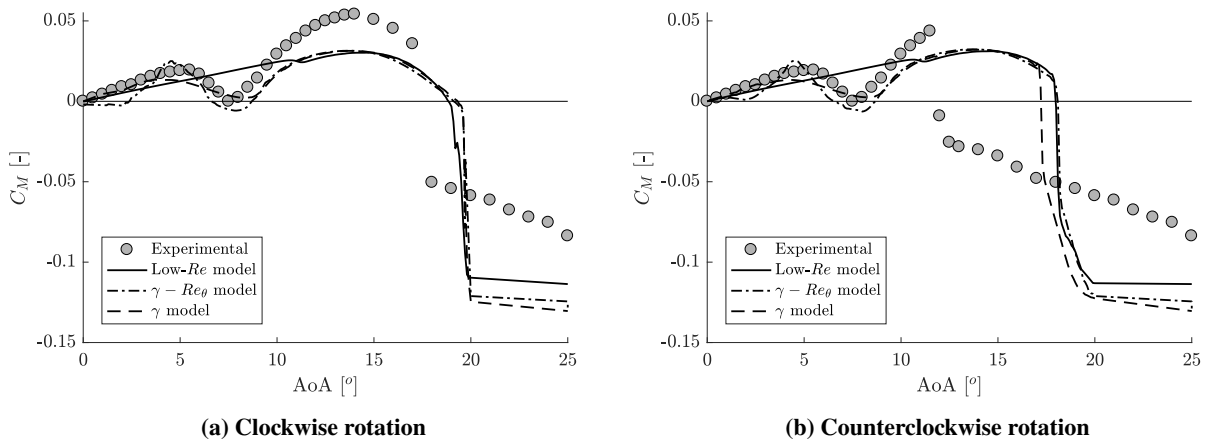


**Fig. 12 Comparison of the  $C_M(\text{AoA})$ -characteristics predicted by the models with experimental data [19]**

Looking at the low- $Re$  model, it can be noted how the over-linear part of the  $C_L$ -characteristic is not predicted. The cause of this is found in the inability of the model to truly predict separation-induced transition: a separation bubble is only modeled to a limited extent. Furthermore, trailing edge separation is predicted to occur much faster than by the other models. This results in the absence of the over-linear part of the  $C_L$ -characteristic and an earlier prediction of the burst angle. Additionally, the model over-predicts most strongly  $C_{L,max}$ , leaving out the  $k - k_l - \omega$  model. Finally, the low- $Re$  model is unable to model hysteresis: the burst angle in clockwise rotation and reattachment angle in counterclockwise rotation are found at the same angle:  $AoA = 18^\circ$ . The different behavior found behind the burst angle for clockwise (see Figure 10a) and counterclockwise (see Figure 10b) rotation is attributed to a lingering transient behavior. This statement was validated through a calculation kept stationary at  $AoA = 19^\circ$  following a clockwise and counterclockwise rotation, which gave the same result.

The  $\gamma$  model shows a behavior somewhat between the low- $Re$  and  $\gamma - Re_\theta$  models: the separation bubble and the over-linear trend are modeled, but not as extensively as in the  $\gamma - Re_\theta$  model. On the other hand the nod between the linear and over-linear part are predicted more correctly. The value of  $C_{L,max}$  is still too large, found between the  $C_{L,max}$  of the low- $Re$  and  $\gamma - Re_\theta$  models. Burst is predicted at the same angle as the  $\gamma - Re_\theta$  model:  $AoA = 19^\circ$ . The most dominating feature of the  $\gamma$  model is found in its prediction of the hysteresis loop: while still far from the experimental value the loop is clearly bigger (Figure 13) compared to other models.

The conclusions drawn in regards to the comparative study of the transition models from  $C_D$  (see Figure 11a and Figure 11b) and  $C_M$  (see Figure 12a and Figure 12b) are more or less identical to those drawn from  $C_L$  and will not be repeated here. However it can be noted that the  $\gamma - Re_\theta$  model predicts  $C_D$  slightly better (is higher compared to the other models) at higher AoAs before burst (see Figure 11a): at  $AoA = 17^\circ$  the difference with the experimental value is 11.5% for the low- $Re$  model, 8.3% for the  $\gamma$  model and 1.0% for the  $\gamma - Re_\theta$  model. This indicates, along with the more correct value of  $C_L$ , the pressure distribution predicted by the  $\gamma - Re_\theta$  model is closer to the experimental one.

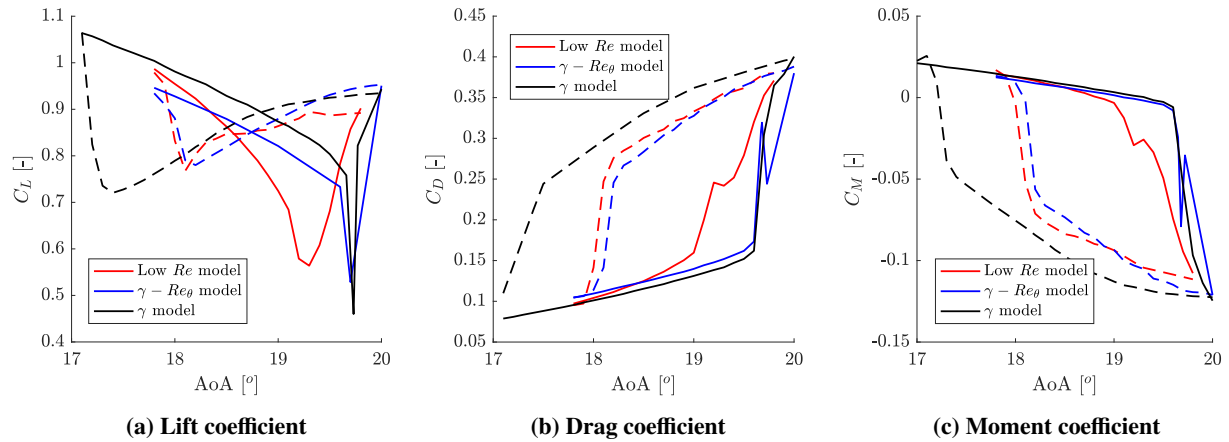


**Fig. 13** Hysteresis loops made up out of the clockwise (full line) and counterclockwise (dashed line) rotations

### III. Quasi-3D Study

The most important conclusions drawn from the 2D study of the transition models for high AoA behavior was the inability of the  $k - k_L - \omega$  model to correctly resolve the flow above  $8^\circ$ , the inability of the low- $Re$  model to predict separation-induced related phenomena and the ability of the  $\gamma - Re_\theta$  and  $\gamma$  models to resolve hysteresis, yet quantitatively wrong. Based on these results will we assess how 3D related phenomena, such as the breakdown of vortices, influences the prediction of hysteresis for the latter two models.

Typically, the characteristics of an airfoil using RANS are assessed in 2D. This simplification can be justified for fully turbulent attached flows where the flow component in the third dimension is predominantly caused by turbulence. In the case of RANS simulations this component is averaged out and represented by the turbulent viscosity  $\mu_t$ . However, in a transitional flow, here in the case of separation-induced transition, the third dimension becomes much more significant since the separation-induced transition process is characterized by the three-dimensional deformation of Kelvin Helmholtz billows and the vortex shedding from the bubble. One can argue that the former is modeled by the production of  $k$  using  $\gamma$ ,  $k_l$  or damping depending on the model, but the latter does not allow the same breakdown process of vortices in 2D as in 3D. This may influence the bubble, possibly its burst behavior, considering its global stability characteristics. Therefore, the transition models are subjected to a comparison between 2D and 3D behavior.

A similar procedure as for the comparison of the two-dimensional flow is followed here: the influence of three-dimensional numerical parameters is examined, which, combined with the numerical parameter study of the two-dimensional flow allow for a three-dimensional grid independent flow domain to be determined, which will then be rotated between an AoA= $0^\circ$  and AoA= $25^\circ$ .

#### A. Boundary Conditions

To allow a direct comparison with the 2D results, a finite span with periodic boundary conditions at both ends is applied. This implies that the computational domain repeats itself an infinite number of times. This eliminates finite wing effects in the shape of wing tip vortices. Measured coefficients are taken using the pressure distribution across the entire surface, not a 2D cross section. As there is still a homogeneous direction, we refer to this study as *quasi-3D*. However, for the sake of legibility, we address it further on as 3D.

#### B. Numerical Parameter Study

For the 3D comparison, the spanwise resolution is examined in order to capture the full spanwise deformation of the separation bubble. The LES of Lardeau, Leschziner & Zaki of a compressor blade in low  $Tu$  and low  $Re$  flow were performed on a grid with a spanwise size of  $0.12c$  in order to capture the Klebanoff streaks that appear even at very low levels of  $Tu$  and the  $\Lambda$ -vortices that they create [24].

However, since it is our intent to assess the behavior of the transition models at high AoAs, possibly with the

appearance of stall cells,<sup>‡‡</sup> which requires a spanwise size corresponding to an AR=2 (aspect ratio is used with caution, since the AR is technically infinite,  $s/c = 200\%$  on Figure 14c), the mesh will be subjected to a spanwise study at three different AoAs:  $0^\circ$ ,  $17^\circ$  and  $25^\circ$  (see Figure 14). The choice of  $\text{AoA}=0^\circ$  is based on observations in 2D, where vortex shedding from the separation bubble is found to be most dominant. The choice of  $\text{AoA}=17^\circ$  is based on the experimental observation of stall cells past the stall angle and before the burst angle, thus, according to Timmer's experimental measurements [19], possibly found at  $\text{AoA}=17^\circ$ . The choice of  $\text{AoA}=25^\circ$  is based on the experimental observation of laminar bluff body separation [23] in the region past the burst angle.

The trends observed at  $\text{AoA}=0^\circ$  go without saying: the three-dimensionality of the flow domain results in a faster breakdown of the vortices translating itself in a smaller amplitude of the fluctuations compared to the 2D case represented by  $s/c = 0\%$ , seen by the decrease in size of the bars, and a smaller mean value caused by a decreased pressure drag (Figure 14a and Figure 14b).

---

<sup>‡‡</sup>Stall cells is the term in literature attributed to the experimentally [23] and numerically [25] observed coherent structures characterized by a strong three dimensional nature of the wake near stall. They appear in the shape of counter-rotating swirl patterns, sometimes also poetically addressed as *owl faces* or *mushroom cells*, through the use of oil flow and tuft measurements. These structures appear in pairs and typically extend spanwise twice the length of the chord. When the span increases beyond AR=2, the cells get stretched before splitting and forming a new pair. The presence of stall cells results in an increased  $C_L$  compared to a fully 2D flow and translates itself in a reduced decrease of  $C_{L,\max}$  following  $C_{L,\max}$ . Overall, the appearance of these cells is limited to a small region of  $\approx 3^\circ$  following  $C_{L,\max}$ .

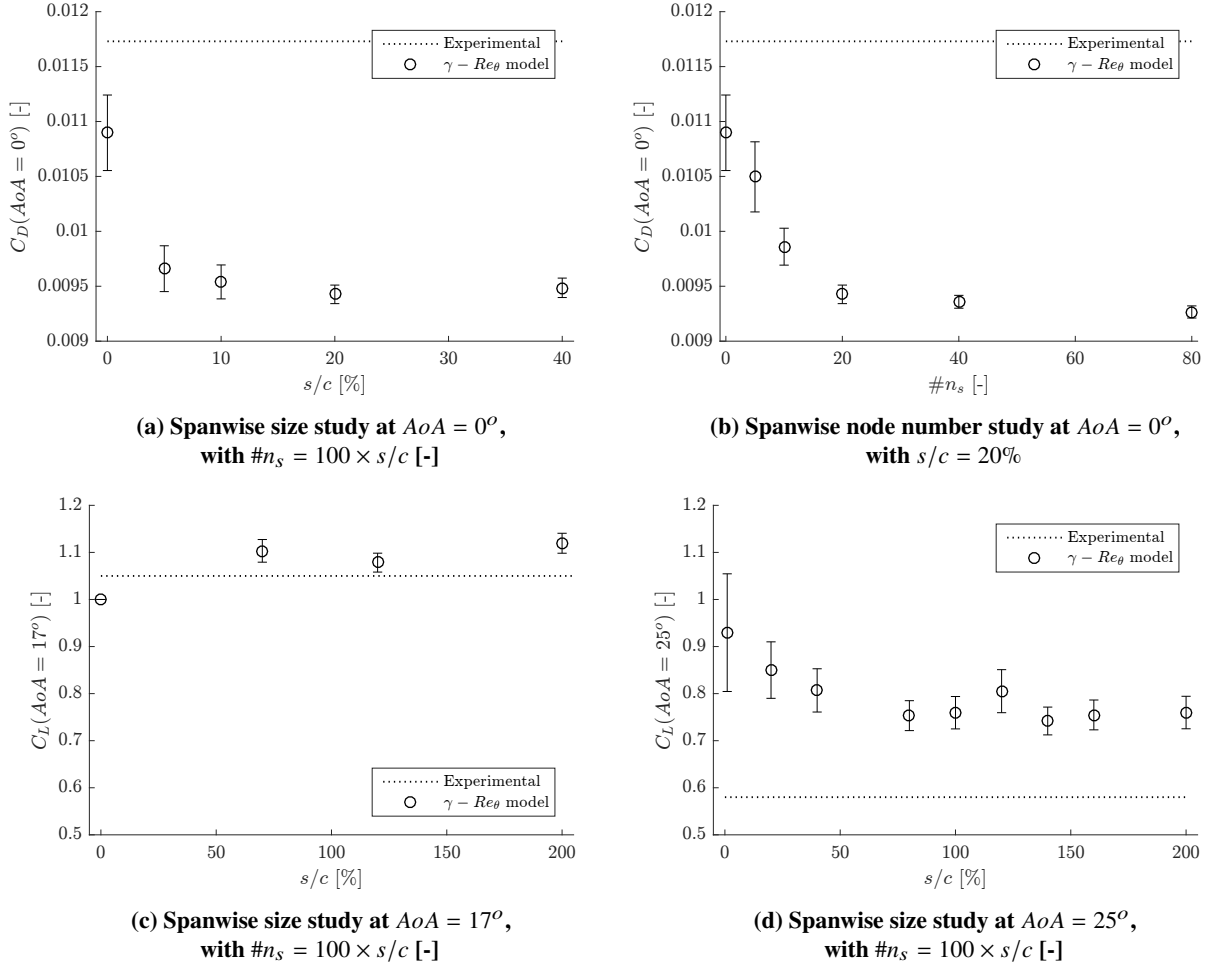


**Fig. 14** Numerical parameter study in 3D using the  $\gamma - Re_\theta$  model presented with error bars of the 95% confidence interval.

At the AoA=17° with  $s/c = 200\%$ : the low- $Re$  model produced a spanwise uniform flow (Figure 18a), while the  $\gamma$  model clearly displays spanwise waviness of its separation front (Figure 18b), unaffected by the vortex shedding from the separation bubble further upstream. The  $\gamma - Re_\theta$  model on the other hand is a prime example of violent vortex shedding from the separation bubble (Figure 18c), breaking up the separation front, which results in a low frequency fluctuating flow (see Figure 21). As illustrated by Broeren & Bragg [26], the time average of the violent shedding flow is two-dimensional, this implies that if the spanwise size ( $s/c$ ) is big enough to fully resolve the breakdown of the vortices, a further increase of the span should yield to the same averaged result. This as opposed to stall cells, which will merge or split if  $s/c$  is changed. This results in a changing  $C_L$  caused by a jet effect between the cells. Figure 14c illustrates that, while there is still some fluctuation left, caused by the time-averaging error due to the low frequency component in the stream, the value of  $C_L$  remains constant even if  $s/c$  is decreased. Noticeable is how the  $C_L$  in 3D is over predicted and in 2D is under predicted.

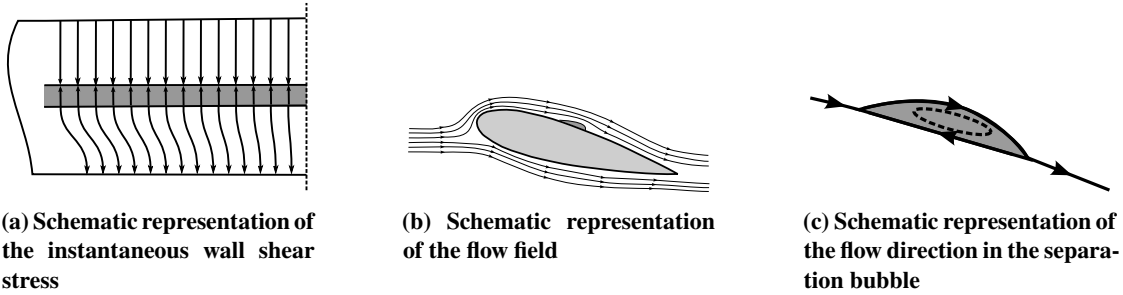


**Fig. 15** Schematics at  $AoA = 8^\circ$  according to the experimental work of Schewe [23].

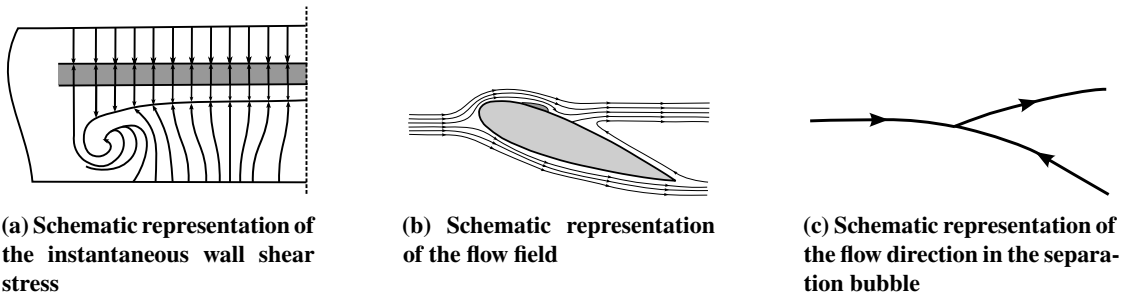


**Fig. 16** Schematics at  $AoA = 12^\circ$  according to the experimental work of Schewe [23].

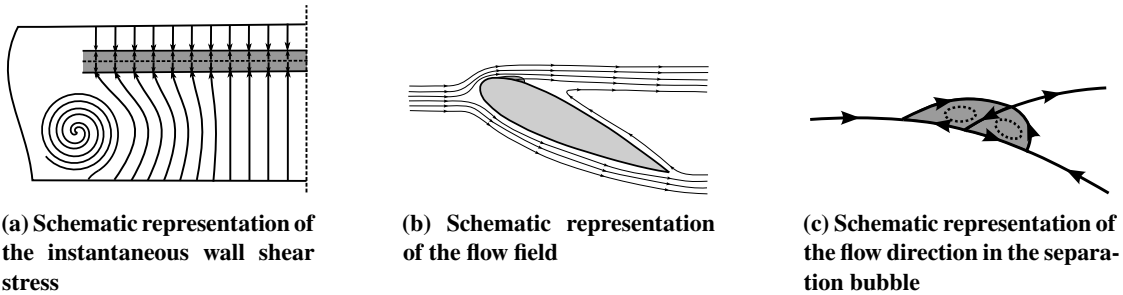
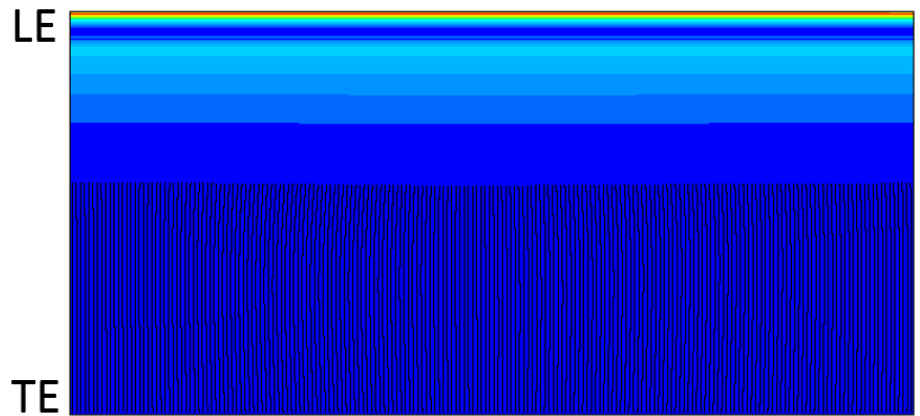


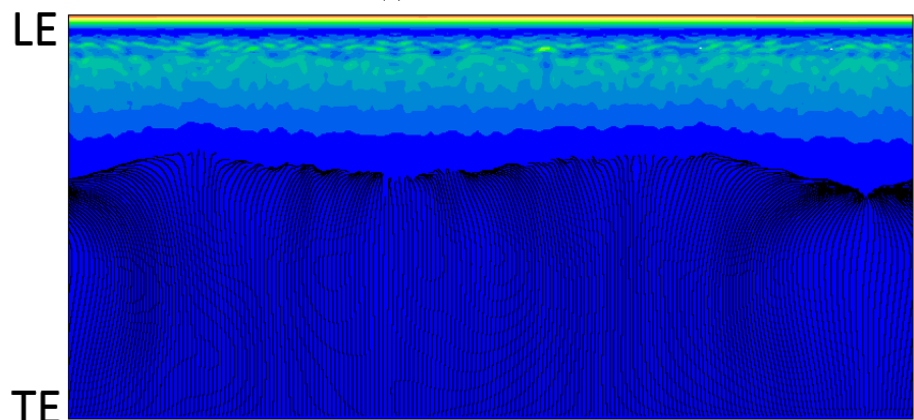
**Fig. 17** Schematics at  $AoA = 17^\circ$  according to the experimental work of Schewe [23].

Once the bubble bursts, the airfoil acts as a bluff body. The experimental work of Schewe [23] (Figures 15,16,17) showed the fundamental difference between the laminar and turbulent flow behind a bluff body. In quantitative terms most noticeable is the much lower  $C_L$  in the laminar case. When considering the flow, the laminar one is predominantly two-dimensional as opposed to its three-dimensional counterpart, which displays a clear periodicity. Figure 14d illustrates the change of span width at  $AoA=25^\circ$ ; noticeable is the increase at  $s/c = 120\%$ . This is caused by the appearance of a second ‘period’ in the spanwise variation of the separated flow which results in a jet effect across the upper side of the airfoil and a subsequent lift increase. From figure 19 the spanwise variation of the separated flow can clearly be noted, indicating that a turbulent flow is predicted as experimentally observed by Schewe (Figure 16).

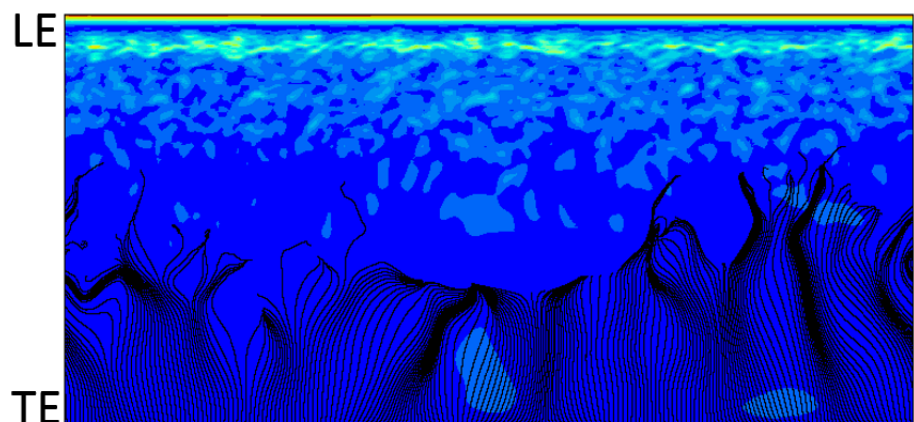
Based on the comparative study it is chosen to perform the 3D simulations with spanwise dicritization using  $s/c = 70\%$  and  $\#n_s = 100 \times s/c [-]$  on top of the 2D mesh that was used in the 2D study. The former is chosen by



(a) low- $Re$  model



(b)  $\gamma$  model



(c)  $\gamma - Re_\theta$  model

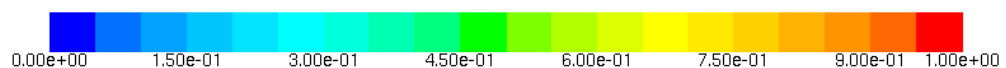


**Fig. 18** Contour plot of the instantaneous wall shear stress on the suction side with oil flow pathlines originating from the trailing edge at AoA=17° with  $s/c = 200\%$ .

considering the results for  $AoA = 25^\circ$ , which show that at  $C_L$  at  $s/c = 70\%$  and  $s/c = 250\%$  are near identical. The latter is to a much lesser extent subjected to the effects of the finite span and thus assumed to be closer to the exact infinite solution. Thus we conclude that at  $s/c = 70\%$  the periodic boundary conditions do not stretch or compress the spanwise period leading to a changing  $C_L$ .

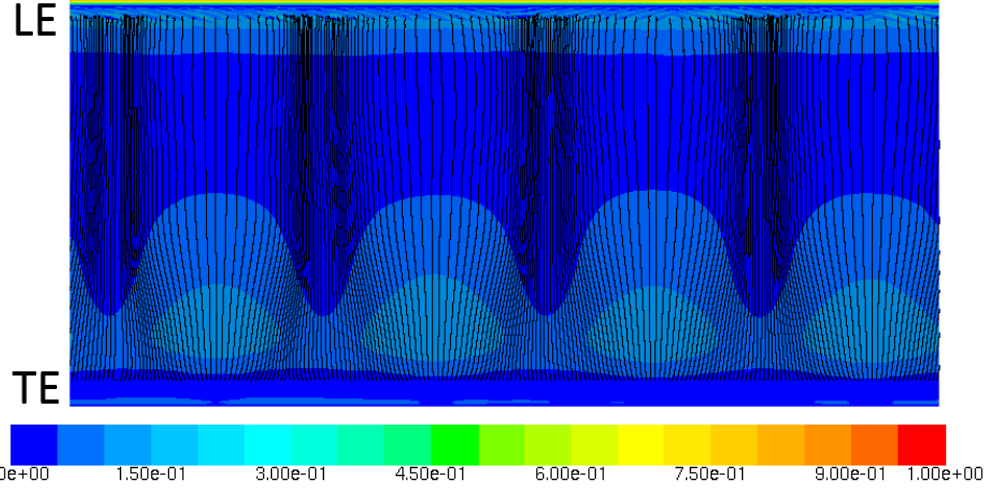


**Fig. 19** Contour plot of the instantaneous wall shear stress on the suction side with oil flow pathlines originating from the trailing edge at  $AoA=25^\circ$  using the  $\gamma - Re_\theta$  model

### C. Results

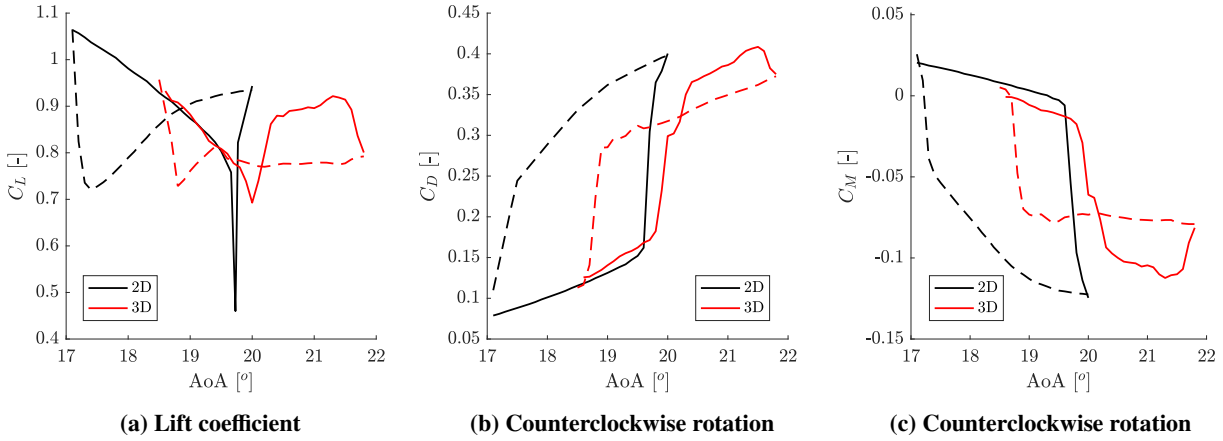
As in the 2D study, first a more in depth comparison of the results of the  $\gamma - Re_\theta$  model with experimental data of the  $C_L$ -,  $C_D$ - and  $C_M$ -characteristics (Figure 21) will be presented, after which the 2D and 3D characteristics of the  $\gamma - Re_\theta$  and  $\gamma$  model will be placed next to each other.

Figure 21a shows the  $C_L$ -characteristic of the  $\gamma - Re_\theta$  model, both in clockwise and counterclockwise rotation, both experimentally and numerically at  $0.1^\circ/s$  ( $1^\circ = 10s$ ). Notable is the absence of a hysteresis loop, the strong over prediction of  $C_{L,max}$  and the presence of high amplitude, low frequency fluctuations between  $AoA = 17^\circ$  and  $22^\circ$ . The latter corresponding to the experimental studies by Broeren & Bragg [26]. With increasing AoA, an increasing amplitude can be seen, reaching  $\Delta C_L \approx 0.6$  at  $AoA = 22^\circ$ . These fluctuations start to appear numerically once experimentally the bubble bursts, followed by the abrupt decrease of  $C_L$ . This opposed to the 2D results (Figure 7a) that show a continuous decrease in lift from  $AoA = 15^\circ$  up to  $AoA = 19.5^\circ$ . These fluctuations are caused by the violent breathing/flapping of the separation bubble and center around the experimental  $C_{L,max} = 1.05$  [19]. Yet this is far above the value that is experimentally predicted in that region:  $C_L \approx 0.6$ . Above  $AoA = 22^\circ$ , the model behaves in accordance to the flow over a bluff body, characterized by much smaller amplitude and much higher frequency fluctuations, with the predicted value corresponding more closely to the experimentally predicted value than in 2D (see Figure 7a). Furthermore, noticeable is the near identical curve for clockwise and counterclockwise rotation, indicating that hysteresis is not predicted in 3D by

the  $\gamma - Re_\theta$  model. It can be argued that the appearance of hysteresis in 2D is related to the restricted vortex breakdown.

Figure 22 shows a comparison of the 2D and 3D central value characteristics predicted by the  $\gamma - Re_\theta$  model. The area of high amplitude low frequency fluctuations is presented as shaded. Besides the above noted deviations, qualitatively the model correctly reproduces the physical phenomena attributed to separation-induced transition. However, on a quantitative level the 2D results correspond more closely to the experimentally measured values at lower AoA, especially in reference to  $C_{L,max}$ .

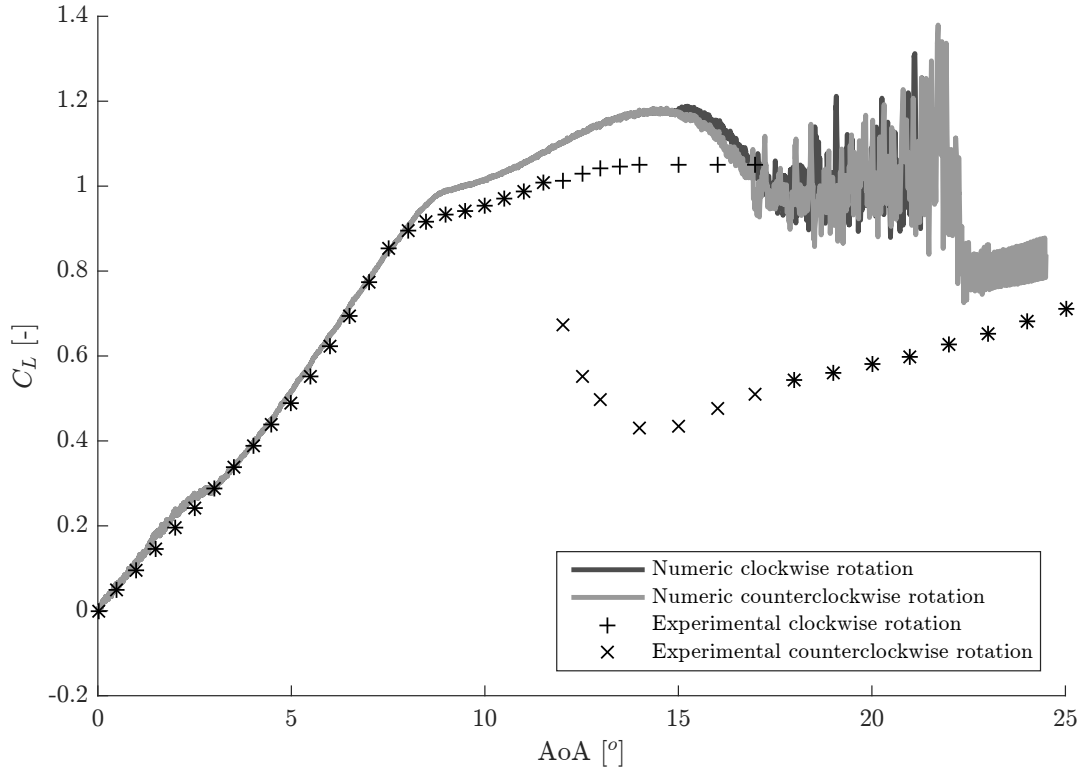
Figure 23 shows a comparison of the 2D and 3D central value characteristics predicted by the  $\gamma$  model. While the  $\gamma$  model is a simplified version of the  $\gamma - Re_\theta$  model, the high AoA behavior predicted by the  $\gamma$  model is distinctly different: the high amplitude, low frequency fluctuations are absent. While  $C_{L,max}$  is, as in the  $\gamma - Re_\theta$  model, more strongly overpredicted in 3D in comparison to 2D, the behavior in clockwise rotation is very similar up to  $AoA = 22^\circ$  with a strong remount of  $C_L$  following the burst angle at  $AoA \approx 19.5^\circ$  due to the 2D bluff body vortex shedding. However, above  $22^\circ$  this shedding becomes 3D leading to a lower predicted  $C_L$  and lying more closely to the experimental value. In counterclockwise direction we find the reattachment angle at a higher value than predicted in 2D. Again, we attribute this to the restricted vortex breakdown in 2D that does not allow an immediate reattachment. However, this reattachment angle is smaller than the burst angle, leaving space for a rather limited hysteresis loop between  $18^\circ$  and  $20^\circ$  (Figure 20).



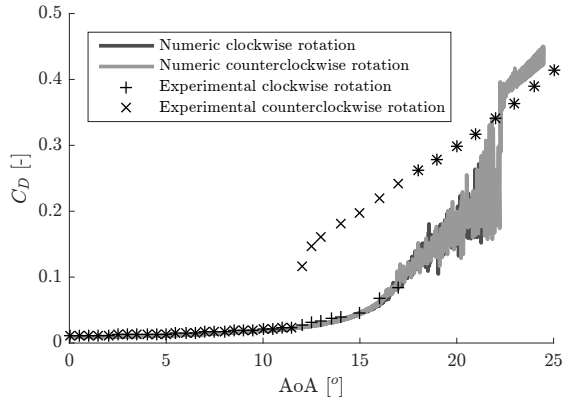
**Fig. 20** Hysteresis loops predicted by the  $\gamma$ -model in 2D and 3D made up out of the clockwise (full line) and counterclockwise (dashed line) rotations

#### IV. Conclusion

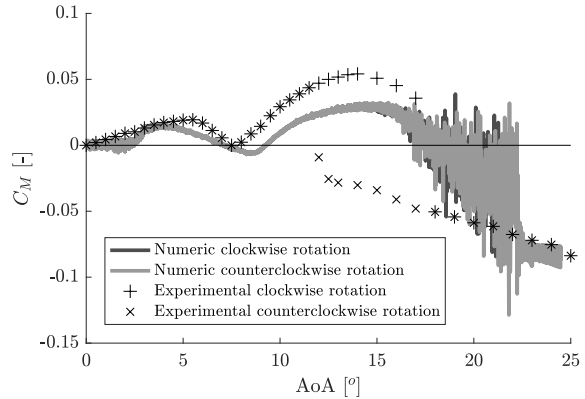
A comparative study of four transition models is presented by studying their capabilities to predict the increased lift caused by the separation bubble at lower AoAs, the abrupt burst of the separation bubble and the accompanied stall at higher AoAs, and the ability to predict (steady) hysteresis. To do this, a NACA 0018 profile is rotated around its mid-chord position at three different rotational speeds with  $Re_c = 3 \times 10^5$ . This allowed an exponential fitting of the



(a)  $C_L(\text{AoA})$ -characteristic

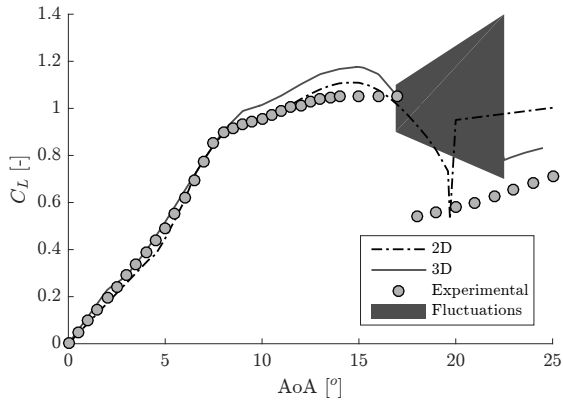


(b)  $C_D(\text{AoA})$ -characteristic

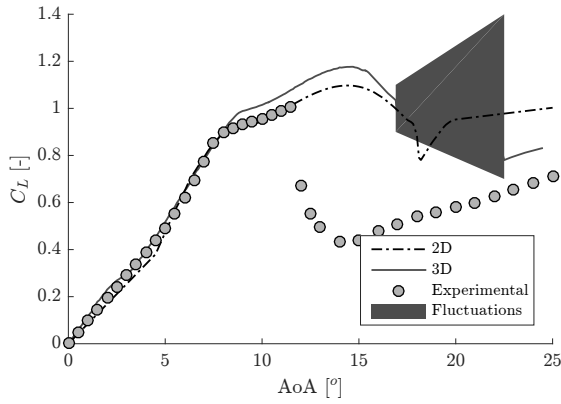


(c)  $C_M(\text{AoA})$ -characteristic

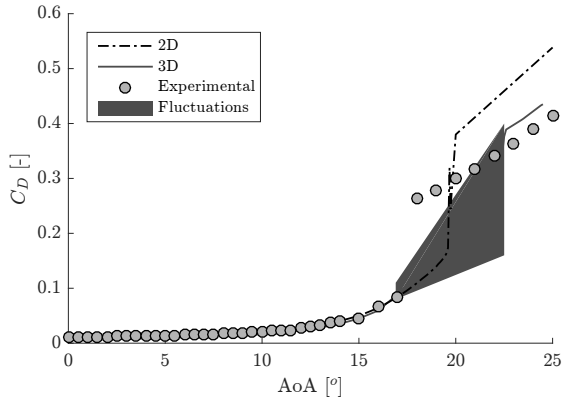
**Fig. 21 Comparison of the characteristics predicted by the  $\gamma - Re_\theta$  model with experimental data [19] in 3D at  $0.1^\circ/\text{s}$**



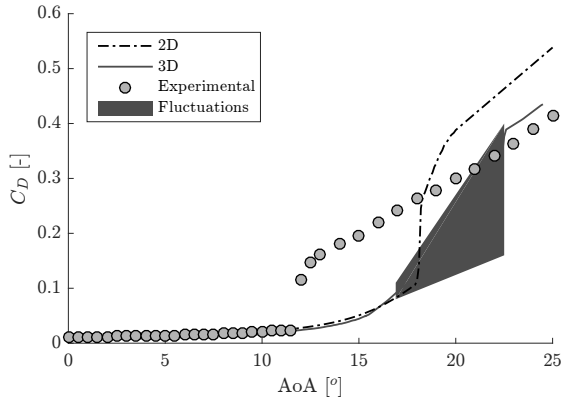
**(a)**  $C_L(AoA)$ -characteristic for clockwise rotation



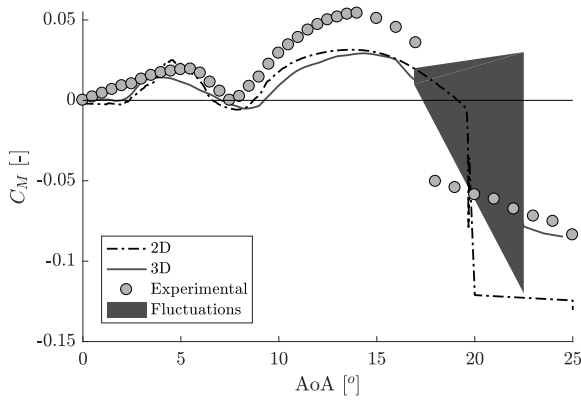
**(b)**  $C_L(AoA)$ -characteristic for counterclockwise rotation



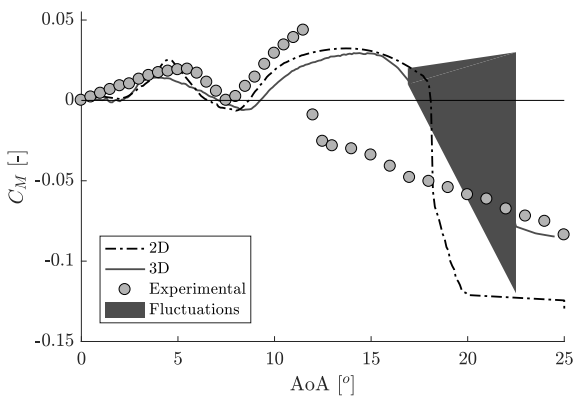
**(c)**  $C_D(AoA)$ -characteristic for clockwise rotation



**(d)**  $C_D(AoA)$ -characteristic for counterclockwise rotation

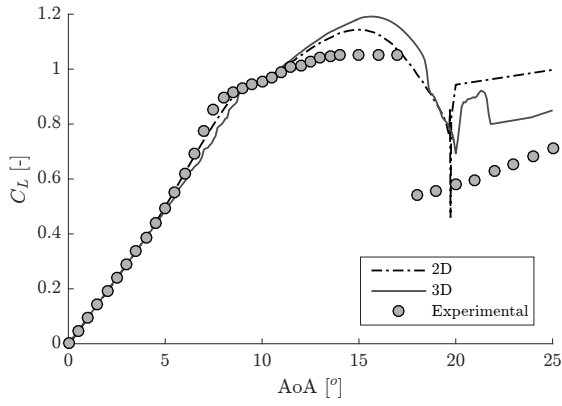


**(e)**  $C_M(AoA)$ -characteristic for clockwise rotation

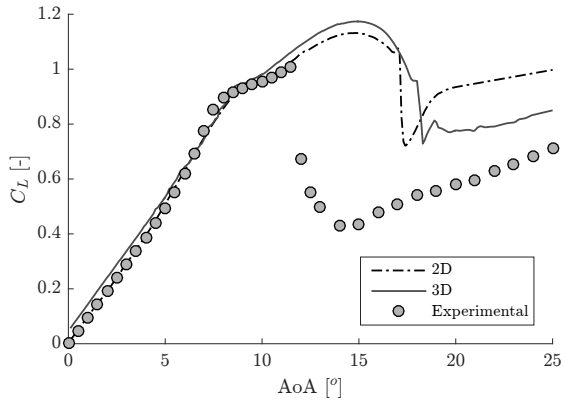


**(f)**  $C_M(AoA)$ -characteristic for counterclockwise rotation

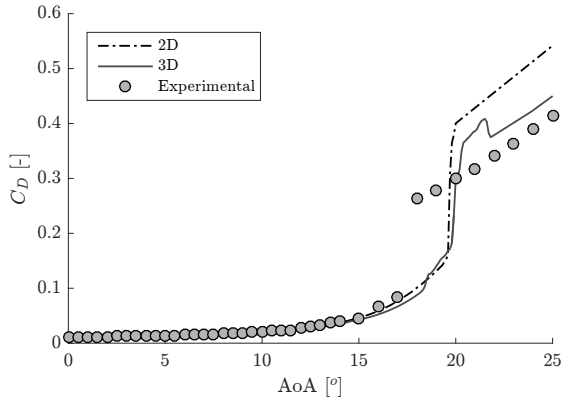
**Fig. 22 Comparison between 2D and 3D characteristics for the  $\gamma - Re_\theta$  model**



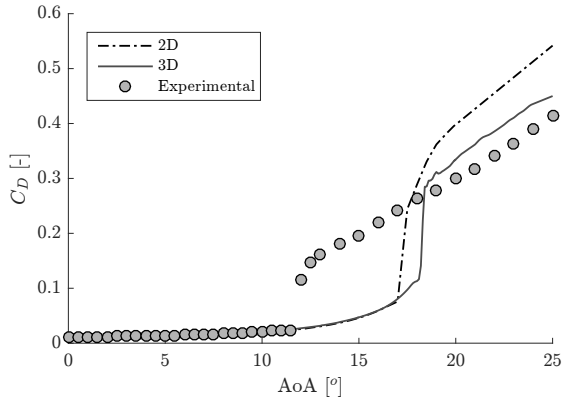
**(a)**  $C_L(AoA)$ -characteristic for clockwise rotation



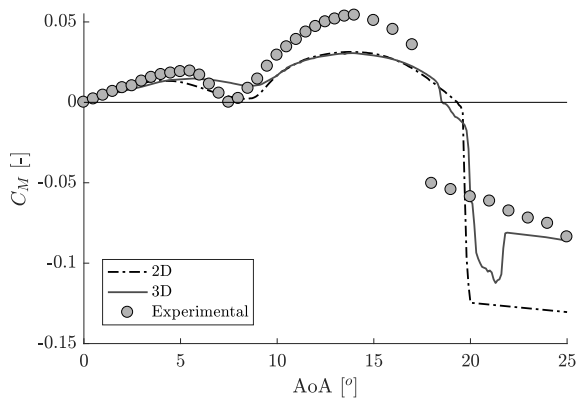
**(b)**  $C_L(AoA)$ -characteristic for counterclockwise rotation



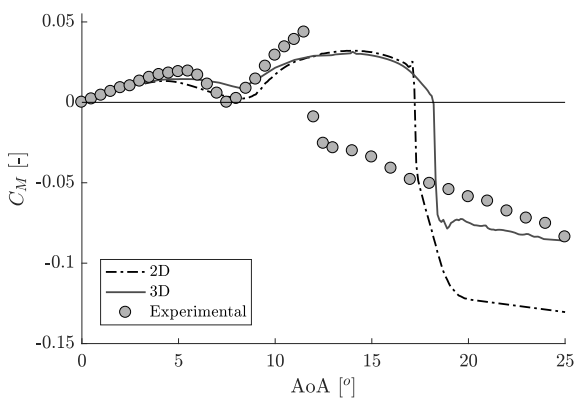
**(c)**  $C_D(AoA)$ -characteristic for clockwise rotation



**(d)**  $C_D(AoA)$ -characteristic for counterclockwise rotation



**(e)**  $C_M(AoA)$ -characteristic for clockwise rotation



**(f)**  $C_M(AoA)$ -characteristic for counterclockwise rotation

**Fig. 23 Comparison between 2D and 3D characteristics for the  $\gamma$  model**

$C_L$ -,  $C_D$ - and  $C_M$ -characteristics and prediction the behavior of a steady simulation for any AoA between  $0^\circ$  and  $25^\circ$ . By doing this the effect of unsteady hysteresis is eliminated. Following the same procedure by rotating counterclockwise from  $25^\circ$  to  $0^\circ$  allowed a quantitative study of the models ability to predict steady hysteresis by comparing them with the experimental results of Timmer [19].

The models were subjected to a mesh and time step sensitivity study, which, along with a *von Neumann* stability analysis, allowed an assessment of the requirements of the mesh and time step to fully resolve the phenomena related to transition: certain combinations of time step and chordal discretization might lead to (i) wrong results and (ii) a steady or unsteady solution, which gives a different value of the integrated quantities. It was further concluded that a minimum of 100 cells in chordwise direction is required to make the separation location independent of discretization, along with a  $y^+$  value of  $\approx 1$ , in agreement with earlier instructions. For the 3D study, caution is in order for the extent of the span depending on the AoA considered: the spanwise size to capture the periodicity in the wake of the bluff body is much larger than required for lower AoAs.

From the 2D study it was concluded that the low- $Re$  model is unable to predict the phenomena that manifest themselves in the  $C_L$ -,  $C_D$ - and  $C_M$ -characteristics as a consequence of the appearance of a separation bubble. The model does predict the stall angle most closely to the experimental value, but does not model the hysteresis loop. The  $\gamma - Re_\theta$ ,  $\gamma$  and  $k - k_l - \omega$  models show a good prediction of the low- $Re$  behavior in the lower  $AoA$ -region. They correctly predict the separation bubble on pressure and suction side and their movement with increasing AoA, which leads to an increase of  $C_M$  up to the point that the separation bubble on the pressure side disappears in the wake resulting in a decrease of  $C_M$  and a stronger increase of  $C_L$ . The  $\gamma - Re_\theta$  model predicted the separation bubble and related phenomena more pronounced than the  $\gamma$  model. With a further increase of the AoA, it was experimentally observed that the boundary layer would start separating from the trailing edge, leading to a stagnation of the  $C_L$  growth and an increase of the  $C_M$ . At this point the  $k - k_l - \omega$  model fails in its predictive capabilities with a delay and under-prediction of separation leading to an increasing  $C_L$ . The  $\gamma - Re_\theta$  and  $\gamma$  models perform better from this point, with the former predicting a  $C_{L,max}$  closer to the experimental value, but strongly over-predicting the burst angle and under-predicting the size of the hysteresis loop. The  $\gamma$  model performed slightly better in the latter case, with a hysteresis loop that is bigger through a later reattachment in the reverse direction. The values of  $C_L$ ,  $C_D$  and  $C_M$  following burst were over-predicted by all models, leading to unphysical values and a *lemniscate*-like shape of the  $C_L$ -hysteresis loop.

From the 3D study it was shown that the  $\gamma - Re_\theta$  model is prone to predict a violent vortex shedding at higher AoA, as opposed to the  $\gamma$  model, which predict a more gently spanwise waviness in the separation front. Experimentally observed stall cells were not found. The fully separated flow is predicted as being completely turbulent, leading to an overestimation of  $C_L$ ,  $C_D$  and  $C_M$  at high AoA, yet closer to the experimental values than the 2D prediction. While present in 2D, the hysteresis loop is not predicted in 3D by the  $\gamma - Re_\theta$  model. The hysteresis does appear in 3D for the  $\gamma$  model, but nowhere near the experimentally predicted region and can thus be considered untrustworthy.

Transition models have proven to be able to model the transition. However, the related effect of hysteresis is not well resolved. Some work has addressed the issue of wrongly prediction of steady/static hysteresis (not only in a low Reynolds context, but also for sharp leading edge airfoils, which are also subjected to this phenomenon) bringing forth some pointer which might pave way to new research and future development of even more capable transition models. Wales et al. divided the numerical approaches within a RANS framework that are able to gain insight into the possible solutions of a nonlinear system as the parameters on which it depends are varied in two: time accurate simulations, as was performed here, and continuations methods [27]. Among the former, a possible solution is the alternative formulation of the turbulence intensity such as in the altered Baldwin-Lomax model, which has proven to be successful in some instances [28, 29]. This is in line with the current ongoing research in transition models. However, another solution is found within the second category, such as for example selective frequency damping (SFD), which forces the flow to a steady solution and allows the assessment of two solutions using continuation methods, thus resolving hysteresis [27, 30].

While modeling of transition has come a long way, the prediction of hysteresis is still an persisting issue. Caution is thus in order when assessing the behavior of UAVs at high angles of attack.

### Acknowledgments

Conducted as part of the SBO research project 140068 EUFORIA (Efficient Uncertainty quantification For Optimization in Robust design of Industrial Applications) under the financial support of the IWT, the Flemish agency of Innovation through Science and Technology. This work was carried out using the STEVIN Supercomputer Infrastructure at Ghent University, funded by Ghent University, the Flemish Supercomputer Center (VSC), the Hercules Foundation and the Flemish Government department EWI.

### Appendix

By means of a *von Neumann* stability analysis (also referred to as *Fourier* stability analysis) it can be assessed whether the change from steady to unsteady behavior by decreasing the time step size can be attributed to the discretization scheme used or should be attributed to the behavior of the transition models. This is done by calculating the amplification factor,  $G$ , as a function of time step size,  $\Delta t$ . We consider a convection-diffusion equation of the transported scalar,  $\phi$  in 1-D under the assumption of a predominantly one directional flow at low AoAs.

$$\frac{\partial}{\partial t}(\rho\phi) + \frac{\partial}{\partial x}(\rho u\phi) = \frac{\partial}{\partial x}\left(\Gamma\frac{\partial\phi}{\partial x}\right) + S_0 - S_1\phi \quad (3)$$

A more generic expression with on the *lhs* the time evolution and on the *rhs* the spatial evolution for an incompressible flow can be presented as:

$$\frac{\partial \phi}{\partial t} = F(\phi) \quad (4)$$

In case of an implicit solver, the spatial function  $F$  is evaluated on time step  $n + 1$  with  $n - 1, n, n + 1$  referring to temporal consecutive steps. The second order time discretization presents itself as follows:

$$\frac{3\phi^{n+1} - 4\phi^n + \phi^{n-1}}{2\Delta t} = F(\phi^{n+1}) \quad (5)$$

Linearizing the above and multiplying  $F$  with  $2\Delta t$  gives  $F^*$ . This results in:

$$3\phi^{n+1} - 4\phi^n + \phi^{n-1} = F^* \phi^{n+1} \quad (6)$$

The amplification factor,  $G$ , is defined as  $\phi^{n+1}/\phi^n = \phi^n/\phi^{n-1} = G$ . Thus we obtain:

$$3 - \frac{4}{G} + \frac{1}{G^2} = F^* \quad (7)$$

Which can be solved for  $G$ :

$$G = \frac{-2 \pm \sqrt{1 + F^*}}{F^* - 3} \quad (8)$$

The amplitude of  $G$  is always smaller than 1 and thus unconditionally stable. We consider the momentum equation, where the transported quantity is velocity, the diffusivity constant,  $\Gamma$ , is equal to  $\mu$  and the source terms are equal to zero. For the spatial discretization of the diffusive term central differencing is used, this gives the following:

$$\frac{2\mu\Delta t}{\rho\Delta x^2} (\phi_{i+1}^{n+1} - 2\phi_i^{n+1} + \phi_{i-1}^{n+1}) \quad (9)$$

With  $i - 1, i, i + 1$  referring to spatially consecutive cells. The coefficient  $(2\mu\Delta t)/(\rho\Delta x^2)$  will be referred to as the diffusive coefficient,  $C_d$ . The convective term uses a second order upwind scheme, this gives the following:

$$-\frac{u\Delta t}{\Delta x} (3\phi_i^{n+1} - 4\phi_{i-1}^{n+1} + \phi_{i-2}^{n+1}) \quad (10)$$

The coefficient  $(u\Delta t)/(\Delta x)$  will be referred to as the convective coefficient,  $C_c$ , and is equal to the *Courant* number. A *Fourier* decomposition of the quantity  $\phi$  is now introduced:  $\phi = \sum_{\omega_F} \phi_{\omega_F} e^{j\omega_F x}$  with  $j$  the imaginary unit,  $\omega_F$  the wavenumber and  $\phi_{\omega_F}$  the wave amplitude. For the diffusive part we obtain (leaving out  $(n+1)$  to retain overview):

$$C_d(\phi_{\omega_F} e^{j\omega_F(x+\Delta x)} - 2\phi_{\omega_F} e^{j\omega_F x} + \phi_{\omega_F} e^{j\omega_F(x-\Delta x)}) \quad (11)$$

Introducing  $F_d$  as the Fourier symbol for the discrete spatial diffusion operator and  $\theta_F = \omega_F \Delta x$ , we obtain:

$$C_d F_d \phi_{\omega_F} e^{j\omega_F x} \quad \text{with} \quad F_d = -2(1 - \cos(\theta_F)) \quad (12)$$

Following the same procedure for the convective term, we obtain:

$$C_c F_c \phi_{\omega_F} e^{j\omega_F x} \quad \text{with} \quad F_c = 3 - 4\cos(\theta_F) + \cos(2\theta_F) + j(4\sin(\theta_F) - \sin(2\theta_F)) \quad (13)$$

Introducing  $F_c$  as the Fourier symbol for the discrete spatial convective operator. On the finest grid size and using the finest time step size it was found that the periodically shed vortices from the separation bubble have an average spatial length on the airfoil of  $\lambda_L = 0.03c$  from which  $\omega_F = 2\pi/\lambda_L$  can be determined. On the finest grid,  $\#n_c = 400$ , it follows that  $\Delta x = c/400$ , from which  $\theta_F = \pi/12$  is obtained. With  $\nu = 1.4607 \times 10^{-6}$  the kinematic viscosity of air and  $u = 5.3682 \text{ m/s}$  the free-stream velocity for  $Re_c = 3 \times 10^5$  and  $c = 1 \text{ m}$ . The amplitude of  $G$  can now be plotted as a function of  $\Delta t$ . Note how two values of  $G$  exist for every  $F$ , however only the branch for which  $G \rightarrow 1$  when  $\Delta t \rightarrow 0$  is considered, corresponding to the minus sign.

It can be seen from the *Bode*-like diagram, Figure 24, how the second order implicit temporal discretization serves as a highpass filter for disturbances as a function of the time step size. For a central differencing scheme of the diffusive terms and a second order upwind scheme for the convective terms a constraint is put on the maximum time step size to resolve the vortex shedding from the separation bubble. The peak values that are seen for the  $k - k_l - \omega$  model around  $-\log_{10}(\Delta t) = 3.7$  ( $\Delta t = 2e^{-4}\text{s}$ ) correspond to the unstable behavior that is found around the pole, leading to incorrect results.

A second order implicit temporal discretization is, apart from the region around the pole for certain  $\Delta t$  and  $\#n_c$  combinations, unconditionally stable. However, the procedure to obtain the results from figure 3b was gradually increasing  $\Delta t$ . Starting at a  $\Delta t$  that was too large undermined the converge of the iterations, thus indirectly imposing a minimum on  $\Delta t$ .

The chordal grid discretization,  $\#n_c$ , (Figure 3a) is strongly related to the time step size and the spatial length of the shed vortices. In order to resolve the vortex shedding it follows that  $\theta \leq \pi$ . At  $AoA = 0^\circ$  this implies that  $\#n_c \geq 67$ . However, near this limit the amplification factor increases strongly above 1 near  $\log_{10}(1/\Delta t) = 3$ , from which an unstable behavior follows.

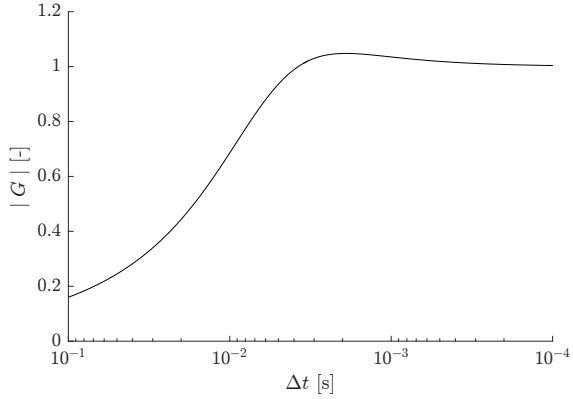


**Fig. 24 Amplitude of the amplification factor as a function of  $\Delta t$ .**

The *von Neumann* stability analysis above illustrates how the discretization scheme used serves as a highpass filter for disturbances as a function of the time step size in the same manner for all unsteady transition model, as seen when comparing figure 3b and figure 24.

## References

- [1] Lissaman, P. B. S., “Low-Reynolds-Number Airfoils,” *Annual Review of Fluid Mechanics*, Vol. 15, No. 1, 1983, pp. 223–239. doi:10.1146/annurev.fl.15.010183.001255, URL <http://dx.doi.org/10.1146/annurev.fl.15.010183.001255>.
- [2] Durbin, P., “An intermittency model for bypass transition,” *International Journal of Heat and Fluid Flow*, Vol. 36, 2012, pp. 1–6. doi:<http://dx.doi.org/10.1016/j.ijheatfluidflow.2012.03.001>, URL <http://www.sciencedirect.com/science/article/pii/S0142727X12000288>.
- [3] Lodefier, K., and Dick, E., “Modelling of Unsteady Transition in Low-Pressure Turbine Blade Flows with Two Dynamic Intermittency Equations,” *Flow, Turbulence and Combustion*, Vol. 76, No. 2, 2006, pp. 103–132. doi:10.1007/s10494-005-9007-1, URL <https://doi.org/10.1007/s10494-005-9007-1>.
- [4] Xu, J., Bai, J., Fu, Z., Qiao, L., Zhang, Y., and Xu, J., “Parallel Compatible Transition Closure Model for High-Speed Transitional Flow,” *AIAA Journal*, Vol. 55, No. 9, 2017, pp. 3040–3050. doi:10.2514/1.J055711, URL <https://doi.org/10.2514/1.J055711>.
- [5] Menter, F. R., “Two-equation eddy-viscosity turbulence models for engineering applications,” *AIAA Journal*, Vol. 32, No. 8, 1994, pp. 1598–1605. doi:10.2514/3.12149, URL <http://dx.doi.org/10.2514/3.12149>.
- [6] Wilcox, D. A., “Simulation of Transition with a Two-Equation Turbulence Model,” *AIAA Journal*, Vol. 32, No. 2, 1994, pp. 247–255. doi:10.2514/3.59994, URL <http://dx.doi.org/10.2514/3.59994>.
- [7] Menter, F. R., Langtry, R. B., Likki, S. R., Suzen, Y. B., Huang, P. G., and Volker, S., “A correlation-based transition model

- using local variables - Part I: Model formulation," *Journal of Turbomachinery-Transactions of the Asme*, Vol. 128, No. 3, 2006, pp. 413–422. doi:10.1115/1.2184352, URL <GotoISI>://WOS:000238562100001.
- [8] Menter, F. R., Smirnov, P. E., Liu, T., and Avancha, R., "A One-Equation Local Correlation-Based Transition Model," *Flow Turbulence and Combustion*, Vol. 95, No. 4, 2015, pp. 583–619. doi:10.1007/s10494-015-9622-4, URL <GotoISI>://WOS:000364930200001.
- [9] Walters, D. K., and Cokljat, D., "A Three-Equation Eddy-Viscosity Model for Reynolds-Averaged Navier-Stokes Simulations of Transitional Flow," *Journal of Fluids Engineering-Transactions of the ASME*, Vol. 130, No. 12, 2008, p. 14. doi:10.1115/1.2979230, URL <GotoISI>://WOS:000260478300009.
- [10] Choudhry, A., Arjomandi, M., and Kelso, R., "A study of long separation bubble on thick airfoils and its consequent effects," *International Journal of Heat and Fluid Flow*, Vol. 52, 2015, pp. 84–96. doi:<http://dx.doi.org/10.1016/j.ijheatfluidflow.2014.12.001>, URL <http://www.sciencedirect.com/science/article/pii/S0142727X14001726>.
- [11] Sanders, D. D., O'Brien, W. F., Sondergaard, R., Polanka, M. D., and Rabe, D. C., "Predicting Separation and Transitional Flow in Turbine Blades at Low Reynolds Numbers – Part II: The Application to a Highly Separated Turbine Blade Cascade Geometry," *Journal of Turbomachinery*, Vol. 133, No. 3, 2010, p. 031011. doi:10.1115/1.4001231, URL <http://dx.doi.org/10.1115/1.4001231>.
- [12] Marty, J., "Numerical investigations of separation-induced transition on high-lift low-pressure turbine using RANS and LES methods," *Proceedings of the Institution of Mechanical Engineers, Part A: Journal of Power and Energy*, Vol. 228, No. 8, 2014, pp. 924–952. doi:10.1177/0957650914548741, URL <http://dx.doi.org/10.1177/0957650914548741>.
- [13] Marxen, O., and Henningson, D. S., "The effect of small-amplitude convective disturbances on the size and bursting of a laminar separation bubble," *Journal of Fluid Mechanics*, Vol. 671, 2011, pp. 1–33. doi:10.1017/s0022112010004957, URL <GotoISI>://WOS:000288100100001.
- [14] Jones, B. M., "Stalling," *The Journal of the Royal Aeronautical Society*, Vol. 38, No. 285, 1934, pp. 753–770. doi:<http://dx.doi.org/10.1017/S0368393100109782>.
- [15] McCullough, G., and Gault, D., "Examples of three representative types of airfoil-section stall at low speed," *NACA Technical Note 2502*, 1951.
- [16] Mueller, T. J., "The influence of laminar separation and transition of low Reynolds-number airfoil hysteresis," *Journal of Aircraft*, Vol. 22, No. 9, 1985, pp. 763–770. doi:10.2514/3.45199, URL <GotoISI>://WOS:A1985APU8100005.
- [17] Williams, D. R., Reißner, F., Greenblatt, D., Müller-Vahl, H., and Strangfeld, C., "Modeling Lift Hysteresis on Pitching Airfoils with a Modified Goman–Khrabrov Model," *AIAA Journal*, Vol. 55, No. 2, 2016, pp. 403–409. doi:10.2514/1.J054937, URL <https://doi.org/10.2514/1.J054937>.

- [18] Ericsson, L. E., and Reding, J. P., “Unsteady Airfoil Stall, Review and Extension,” *Journal of Aircraft*, Vol. 8, No. 8, 1971, pp. 609–616. doi:10.2514/3.59146, URL <http://dx.doi.org/10.2514/3.59146>.
- [19] Timmer, W., “Two-Dimensional Low-Reynolds Number Wind Tunnel Results for Airfoil NACA 0018,” *Wind Engineering*, Vol. 32, No. 6, 2008, pp. 525–537. doi:10.1260/030952408787548848.
- [20] Spalart, P. R., and Rumsey, C. L., “Effective Inflow Conditions for Turbulence Models in Aerodynamic Calculations,” *AIAA Journal*, Vol. 45, No. 10, 2007, pp. 2544–2553. doi:10.2514/1.29373, URL <http://dx.doi.org/10.2514/1.29373>.
- [21] Langtry, R. B., Menter, F. R., Likki, S. R., Suzen, Y. B., Huang, P. G., and Volker, S., “A correlation-based transition model using local variables - Part II: Test cases and industrial applications,” *Journal of Turbomachinery-Transactions of the Asme*, Vol. 128, No. 3, 2006, pp. 423–434. doi:10.1115/1.2184353, URL <Go to ISI>://WOS:000238562100002.
- [22] Driver, D. M., Seegmiller, H. L., and Marvin, J. G., “Time-dependent behavior of a reattaching shear layer,” *AIAA Journal*, Vol. 25, No. 7, 1987, pp. 914–919. doi:10.2514/3.9722, URL <http://dx.doi.org/10.2514/3.9722>.
- [23] Schewe, G., “Reynolds-number effects in flow around more-or-less bluff bodies,” *Journal of Wind Engineering and Industrial Aerodynamics*, Vol. 89, No. 14–15, 2001, pp. 1267–1289. doi:[http://doi.org/10.1016/S0167-6105\(01\)00158-1](http://doi.org/10.1016/S0167-6105(01)00158-1), URL <http://www.sciencedirect.com/science/article/pii/S0167610501001581>.
- [24] Lardeau, S., Leschziner, M., and Zaki, T., “Large Eddy Simulation of Transitional Separated Flow over a Flat Plate and a Compressor Blade,” *Flow Turbulence and Combustion*, Vol. 88, No. 1-2, 2012, pp. 19–44. doi:10.1007/s10494-011-9353-0, URL <Go to ISI>://WOS:000299370700003.
- [25] Manolesos, M., Papadakis, G., and Voutsinas, S. G., “Experimental and computational analysis of stall cells on rectangular wings,” *Wind Energy*, Vol. 17, No. 6, 2014, pp. 939–955. doi:10.1002/we.1609, URL <http://dx.doi.org/10.1002/we.1609>.
- [26] Broeren, A. P., and Bragg, M. B., “Spanwise Variation in the Unsteady Stalling Flowfields of Two-Dimensional Airfoil Models,” *AIAA Journal*, Vol. 39, No. 9, 2001, pp. 1641–1651. doi:10.2514/2.1501, URL <http://dx.doi.org/10.2514/2.1501>.
- [27] Wales, C., Gaitonde, A. L., Jones, D. P., Avitabile, D., and Champneys, A. R., “Numerical continuation of high Reynolds number external flows,” *International Journal for Numerical Methods in Fluids*, Vol. 68, No. 2, 2010, pp. 135–159. doi:10.1002/fld.2497, URL <https://doi.org/10.1002/fld.2497>.
- [28] Mittal, S., and Saxena, P., “Prediction of Hysteresis Associated with the Static Stall of an Airfoil,” *AIAA Journal*, Vol. 38, No. 5, 2000, pp. 933–935. doi:10.2514/2.1051, URL <https://doi.org/10.2514/2.1051>.
- [29] Sereez, M., Abramov, N., and Goman, M., “Computational Simulation of Airfoils Stall Aerodynamics at Low Reynolds Numbers,” Royal Aeronautical Society, Applied Aerodynamics Conference, ????
- [30] Richez, F., Leguille, M., and Marquet, O., “Selective frequency damping method for steady RANS solutions of turbulent separated flows around an airfoil at stall,” *Computers & Fluids*, Vol. 132, 2016, pp. 51–61. doi:<https://doi.org/10.1016/j.compfluid.2016.03.027>, URL <http://www.sciencedirect.com/science/article/pii/S0045793016300871>.